
Regionality and seasonality of submesoscale and mesoscale turbulence in the North Pacific Ocean

Sasaki Hideharu ^{1,*}, Klein Patrice ², Sasai Yoshikazu ³, Qiu Bo ⁴

¹ Application Laboratory, JAMSTEC Yokohama, Japan

² Laboratoire d'Océanographie Physique et Spatiale, IFREMER-CNRS-UBO-IRD Plouzane, France

³ Research and Development, Center for Global Change JAMSTEC Yokohama, Japan

⁴ Department of Oceanography, University of Hawaii at Manoa Honolulu, USA

* Corresponding author : Hideharu Sasaki, email address : sasaki@jamstec.go.jp

Abstract :

The kinetic energy (KE) seasonality has been revealed by satellite altimeters in many oceanic regions. Question about the mechanisms that trigger this seasonality is still challenging. We address this question through the comparison of two numerical simulations. The first one, with a 1/10° horizontal grid spacing, 54 vertical levels, represents dynamics of physical scales larger than 50 km. The second one, with a 1/30° grid spacing, 100 vertical levels, takes into account the dynamics of physical scales down to 16 km. Comparison clearly emphasizes in the whole North Pacific Ocean, not only a significant KE increase by a factor up to three, but also the emergence of seasonal variability when the scale range 16–50 km (called submesoscales in this study) is taken into account. But the mechanisms explaining these KE changes display strong regional contrasts. In high KE regions, such the Kuroshio Extension and the western and eastern subtropics, frontal mixed-layer instabilities appear to be the main mechanism for the emergence of submesoscales in winter. Subsequent inverse kinetic energy cascade leads to the KE seasonality of larger scales. In other regions, in particular in subarctic regions, results suggest that the KE seasonality is principally produced by larger-scale instabilities with typical scales of 100 km and not so much by smaller-scale mixed-layer instabilities. Using arguments from geostrophic turbulence, the submesoscale impact in these regions is assumed to strengthen mesoscale eddies that become more coherent and not quickly dissipated, leading to a KE increase.

Keywords : Submesoscale turbulence, Scale interactions, Mixed-layer instability, High-resolution simulations, North Pacific

47 **1 Introduction**

48 Oceanic eddies (100-300 km) have been monitored by satellite altimeters for more
49 than 25 years. They are now known to explain, not only most of the total ocean kinetic energy
50 (KE) (Ferrari and Wunsch 2009), but also most of the turbulent dispersion and transport of
51 tracers such as heat and carbon dioxide in the global ocean (Lévy et al. 2012a; Haza et al.
52 2012; Zhong and Bracco 2013). Altimeter data further reveal, in many regions, the existence
53 of significant seasonality of the kinetic energy associated with these mesoscale eddies (Eddy
54 Kinetic Energy or EKE) (Qiu 1999; Zhai et al. 2008; Dufau et al. 2016), often 180° out of
55 phase with the atmospheric forcing (Zhai et al 2008; Dufau et al. 2016). This has led to
56 question the mechanisms leading to this EKE seasonality

57 A first answer has been proposed by several studies (Qiu 1999; Qiu et al. 2008;
58 Capet et al. 2016) invoking the baroclinic instability of large-scale vertical current shears in
59 the upper oceanic layers with a wavelength of the order of 100 km (see Tulloch et al. 2011).
60 Their explanation is based on the thermocline tilt change caused by the atmospheric forcings.
61 Specifically, Qiu (1999) and Qiu et al. (2008) showed that, in the subtropical gyre of the
62 North Pacific Ocean, the well-stratified upper thermocline in summer/fall is destroyed in
63 winter because of the surface cooling that begins in late October. This leads the upper
64 thermocline tilt to be enhanced and reach a maximum in early spring with an associated
65 increased vertical shear, a favorable situation for a Charney-type baroclinic instability to
66 develop. When the surface buoyancy forcing changes from cooling to heating, a flatter
67 seasonal thermocline builds up, which weakens the vertical shear and therefore inhibits
68 baroclinic instability. Qiu (1999) and Qiu et al. (2008) further noted, using altimeter data, that
69 the EKE also experiences a seasonal cycle but with a phase lag of about 2 months behind the

70 seasonal cycle of the thermocline tilt. Analysis of the Argo and altimetry datasets suggests a
71 similar scenario for the density structure south of the Gulf Stream (Capet et al. 2016).

72 Another explanation invokes the impact of scales smaller than 50 km (called
73 submesoscales in the present study). These scales usually emerge, preferentially in winter,
74 from the instabilities of surface frontal structures (Thompson et al. 2016). Many recent studies
75 suggest mixed-layer instability - with typical unstable wavelengths of 10–40 km - (MLI, see
76 Boccaletti et al. 2007; Fox Kemper et al. 2008; Callies et al. 2016) as the main mechanism
77 explaining the emergence of submesoscales in winter (Capet et al 2008a; Mensa et al 2013;
78 Qiu et al. (2014); Sasaki et al. (2014) [hereafter respectively Q14 and S14]; Callies et al.
79 2016). They further show that the resulting kinetic energy at submesoscales subsequently
80 cascades to larger scales leading to a maximum EKE around May-June. The resulting EKE
81 spectra are characterized by a winter k^{-2} slope (with k the wavenumber) and a summer k^{-3}
82 slope (Q14; S14). Callies et al. (2015) using ADCP data in the Gulf Stream region reported
83 similar results involving EKE spectra with a k^{-2} slope in winter and a k^{-3} slope in summer,
84 suggesting the presence of more energetic submesoscales in winter.

85 The present study focuses on the mechanisms that trigger the EKE seasonality in
86 the North Pacific Ocean (NPO). For that purpose, we compare the results of two numerical
87 simulations (described in section 2), identical except for the resolution. The first one, with a
88 $1/10^\circ$ horizontal resolution (with 54 vertical levels), does not resolve scales below 50 km and
89 therefore does not take into account submesoscales. The second one, with a $1/30^\circ$ horizontal
90 resolution (with 100 vertical levels) resolves a large part of the submesoscale range (between
91 16 km and 50 km). As shown in section 3, the two simulations display quite different results,
92 in terms of both magnitude and seasonality, for the relative vorticity, mixed-layer depth

93 (MLD) and EKE fields. Section 4 indicates that, in regions with high EKE - mostly the
94 Kuroshio Extension and subtropics, the seasonality of the ocean dynamics is principally
95 driven by the winter submesoscales. Discussion in section 5 suggests that, in other regions
96 where EKE is lower, the seasonality of the ocean dynamics is principally driven by larger-
97 scale instabilities. Discussion is offered in the last section.

98

99 **2. Two numerical simulations of the North Pacific Ocean**

100 The OGCM for the Earth Simulator (OFES) model (Masumoto et al. 2004; Komori
101 et al. 2005) is used to conduct two hindcast simulations at $1/30^\circ$ (Sasaki and Klein 2012; S14)
102 and at $1/10^\circ$ (Nonaka et al. 2016) horizontal resolutions [hereafter referred to as the $1/30^\circ$
103 simulation and $1/10^\circ$ simulation, respectively]. This model is based on MOM3 (Pacanowski
104 and Griffies 1999), a hydrostatic ocean model subject to Boussinesq and hydrostatic
105 approximations. The number of vertical levels is 100 (54) for the $1/30^\circ$ ($1/10^\circ$) simulation. A
106 bi-harmonic operator damps numerical noises and vertical mixing makes use of a scheme
107 developed by Noh and Kim (1999). Bi-harmonic viscosity and diffusion coefficients are
108 respectively $1.0 \times 10^9 \text{ m}^4 \text{ s}^{-1}$ ($2.7 \times 10^{10} \text{ m}^4 \text{ s}^{-1}$) and $3.3 \times 10^8 \text{ m}^4 \text{ s}^{-1}$ ($9.0 \times 10^9 \text{ m}^4 \text{ s}^{-1}$) in the $1/30^\circ$
109 ($1/10^\circ$) simulation. The model domain covers the North Pacific Ocean with a meridional
110 coverage from 20°S to 68°N and a zonal coverage from 100°E to 70°W . The climatological
111 integration of the $1/10^\circ$ simulation for 15 years was first conducted by using long-term mean
112 6-hourly atmospheric data from 1979 to 2004 of Japanese 25-year reanalysis (Onogi et al.
113 2007). The hindcast simulation from 1979 to 2012 followed this climatological simulation.
114 The $1/30^\circ$ simulation started from the regridded output of the $1/10^\circ$ simulation on January 1,
115 2000 and ended on December 31, 2003. The spin-up period for the upper ocean circulation for

116 the $1/30^\circ$ simulation is less than one year. Consequently, only outputs from the period from
117 January 1, 2001 to December 31, 2003 are analyzed in this study.

118 A numerical simulation with a given horizontal resolution, allows to capture
119 correctly the physics of wavelengths of at least 5 times this resolution (Lévy et al. 2012b).
120 This means that the $1/10^\circ$ and $1/30^\circ$ simulations capture the physics of wavelengths
121 respectively larger than 50 km and 16 km. KE associated with submesoscales (< 50 km) is
122 known to result from mechanisms such as frontogenesis, wind-driven frontal instabilities,
123 mixed-layer instabilities (MLIs) and others (see Haines and Marshall, 1998; McWilliams
124 2016; Thompson et al. 2016). Observational studies further emphasize that these instabilities
125 are mostly efficient in winter and negligible in summer (Thompson et al. 2016; Buckingham
126 et al. 2016). At last, many studies (Q14; S14; Callies et al. 2016; Thompson et al. 2016)
127 suggest that winter submesoscales are mostly generated by MLI because of the larger mixed-
128 layer depth (MLD) during this period (Boccaletti et al. 2007; Fox-Kemper et al. 2008). To
129 better understand whether our two simulations resolve or not MLIs, we have estimated the
130 most unstable MLI wavelengths (Stone, 1966; Nakamura, 1988) in the whole NPO as a
131 function of time using the same method as in Fox-Kemper et al. (2008) (see also S14).
132 Figures 1a-c indicate winter values (December through February) larger than 20-25 km.
133 These wavelengths are well resolved in the $1/30^\circ$ simulation but not in the $1/10^\circ$ simulation.
134 Consequently, comparison between the two simulations allows to diagnose the impacts of the
135 winter “MLI” submesoscales on the NPO ocean dynamics. All the dynamical fields analyzed
136 in the next sections have been averaged over a one day period in order to filter out near-
137 inertial motions.

138

139 **3 Basin-scale impacts of submesoscales**

140 Surface frontal structures are usually associated with intensified along-front jets and
141 therefore are often exhibited in the relative vorticity (RV) field. In such frontal dynamics, RV
142 characterizes the size of these structures and their dynamics since smaller-scale surface frontal
143 structures exhibit larger RV (Held et al. 1995) (and therefore larger Rossby number, Ro , with
144 Ro defined as $Ro = \zeta/f$, ζ being the relative vorticity and f the Coriolis frequency), leading to
145 large vertical velocities (Klein and Lapeyre 2009).

146 Figures 2a,b reveal the emergence of a strong and conspicuous seasonality in the
147 RV field of the $1/30^\circ$ simulation. This seasonality is characterized by much smaller scales
148 with larger amplitudes in winter (with Ro reaching values of order one) compared to summer,
149 suggesting the presence of energetic submesoscales in winter. However, this seasonality has
150 not the same intensity everywhere. The northern part of the NPO and some areas in the
151 eastern part have much weaker Ro magnitude but still exhibit a non-negligible seasonality as
152 discussed later. On the other hand, no seasonality is observed in the $1/10^\circ$ simulation in which
153 the RV field displays much weaker amplitudes and larger scales (Figures 2 c,d).

154 It is well recognized, since Hakim et al. (2002), that the submesoscale turbulence
155 triggered by surface frontal instabilities (including MLI) leads to positive (up-gradient)
156 buoyancy fluxes and therefore to a restratification of the upper oceanic layers (Lapeyre et al.
157 2006; Boccaletti et al. 2007 ; Fox Kemper et al. 2008; McWilliams et al. 2009 ; S14 ; Callies
158 et al. 2016). To further characterize this impact, we have compared the winter MLD¹ fields in
159 both simulations. Areas with large MLD (> 200 m) (Figures 3a,b) are patchy to the south and
160 north of the Kuroshio Extension region (KET), which is consistent with the hydrographic and

¹ The MLD is defined as the depth at which potential density is different from the sea surface density by $0.03 \sigma_\theta$.

161 Argo floats observations (Suga et al. 2004; de Boyer Montegut 2009). In the eastern
162 subtropical region (around 140°W and 25°N) where the subtropical mode water is ventilated
163 (e.g. Hautala and Roemmich 1998; Hanawa and Tally 2001), MLD is deep compared with the
164 surroundings, which is also consistent with observations. The submesoscale impact on the
165 restratification is revealed by Figure 3c that shows the winter MLD differences between the
166 two simulations. In KET, the subtropical regions and also the mid-latitude region in the
167 eastern part, MLD is shallower in the 1/30° simulation than in the 1/10° simulation (with a
168 difference that can exceed 100 m). This highlights a strong restratification impact in regions
169 where large RV magnitude with a strong seasonality is observed (Figures 2a,b). However, in
170 the northern parts of the NPO (west and east), in particular in the northern part of the
171 Kuroshio Extension, MLD is conspicuously larger in the 1/30° simulation, indicating
172 submesoscales contribute to deepen the mixed-layer instead of shallowing it.

173 The positive buoyancy fluxes, associated with submesoscales, also correspond to a
174 net transformation of potential energy (PE) into KE. Some studies (Fox-Kemper et al. 2008;
175 Q14; S14; Callies et al. 2016) further suggest that this KE flux at submesoscales is transferred
176 to larger scales (through the inverse KE cascade) and therefore feeds up KE of mesoscale
177 eddies. Therefore, it is pertinent to question the EKE differences between our two simulations.
178 Figures 4a,b display the EKE, averaged over the 2001-2003 period, in both simulations, with
179 Figure 4c showing the EKE difference. In agreement with satellite altimeter observations
180 (Zhai et al. 2008), Figures 4a,b display a high EKE level along the KET region, a moderate
181 level in subtropical regions including along the Subtropical Countercurrent (STCC) (EKE is
182 reduced by a factor 2 to 4 compared with the KET region), and a lower level (reduced by a
183 factor 10) in other areas including the subarctic and eastern mid-latitude regions. But Figure

184 4c reveals that, taking into account submesoscales, leads to an EKE increase by a factor close
185 to 2 in the KET and western and eastern subtropical regions. Other regions with smaller EKE
186 experience as well an EKE increase (with also a factor 2) in the $1/30^\circ$ simulation, but this
187 increase is not so well displayed in Figure 4c because of the color scale. The factor 2 increase
188 is consistent with the results from similar numerical experiments in the North Atlantic Ocean
189 designed to assess the impact of small scales (E. Chassignet, personal communication).
190 Furthermore, in all regions of the NPO, EKE time evolution (Fig. 5) reveals a significant
191 seasonality in the $1/30^\circ$ simulation, with a spring-summer maximum, consistent with satellite
192 observations (Zhai et al 2008; Dufau et al. 2016). No EKE seasonality is observed in the
193 $1/10^\circ$ simulation.

194 These EKE results point to the pertinence of the question raised in the introduction:
195 which mechanisms associated with submesoscales (16-50 km) trigger the EKE seasonality
196 and EKE magnitude increase. Figures 1-4 emphasize the existence of two classes of regions
197 in the NPO: regions with large EKE and energetic submesoscales (large RV values) leading
198 to a mixed-layer shallowing and others, with weaker EKE and less energetic submesoscales
199 leading to a weaker ML shallowing or to a mixed-layer deepening. We next address this
200 question in each of these two classes. Our analyses are conducted in six specific regions
201 sketched in Figure 1a: three of them corresponding to the first class - namely the Kuroshio
202 Extension (KET), Subtropical Countercurrent (STCC), Subtropical Eastern Pacific (STEP)
203 regions - and the other three corresponding to the second class - namely the Mid-Latitude
204 Eastern Pacific (MLEP), Subarctic Western Pacific (SAWP), and Subarctic Eastern Pacific
205 (SAEP) regions.

206

207 4. Impacts of submesoscales in high EKE regions

208 The first three regions (KET, STCC, and STEP) experience a significant RV
209 seasonality in the $1/30^\circ$ simulation with Ro_{rms} values up to 0.2 and seasonal amplitude
210 varying with a factor 1.5 to 2 between winter and summer (Figures 6a-c). The vertical
211 velocity (W) time series exhibit a similar seasonality with a factor 3 amplitude. On the other
212 hand, without submesoscales ($1/10^\circ$ simulation), these two quantities conspicuously display
213 almost no or a very weak seasonality. Not surprisingly, the MLD exhibits a strong seasonality
214 in both simulations, but its winter magnitude is smaller in the $1/30^\circ$ simulation as already
215 noted in Figure 3. As in S14, there is a lag of about one month between RV and MLD (and
216 W) time series: MLD and W time series exhibit a similar seasonality and a sudden decay in
217 late winter not observed for RV. One explanation (see S14 for details) is that the RV field,
218 after the abrupt decay of MLD and W , evolves as a two-dimensional turbulent flow in free-
219 decay. Figure 7 shows meridional sections of W in winter respectively in the western and
220 eastern parts of the North Pacific Ocean. They illustrate the larger magnitude but also the
221 smaller scales of this field in the $1/30^\circ$ simulation compared to the $1/10^\circ$ simulation. They
222 also emphasize that W involves smaller scales in upper layers than in deeper layers. These
223 results suggest that MLD drives the RV evolution (Figures 6a-c) and therefore the production
224 of small scales.

225 Characteristics of these time series in winter, in particular their phase relationship
226 strongly suggest MLI as the main mechanism explaining the emergence of submesoscales in
227 the $1/30^\circ$ simulation. Indeed, the most unstable MLI wavelength in the first three regions
228 (KET, STCC, and STEP) is larger than 20-30 km in winter (Figures 1) except in a small area
229 close to Japan where it is smaller. To confirm this in all three regions, we plotted the time

230 series of the buoyancy fluxes ($\langle w'b' \rangle_{xy}$ with w' , b' and $\langle * \rangle_{xy}$ respectively the vertical
231 velocity, buoyancy anomaly, and horizontal average operator over each region) as a function
232 of depth (Figure. 8). The buoyancy fluxes represent the transformation of PE into KE. The
233 flux is mostly positive and strongly intensified within the mixed-layer with a larger magnitude
234 in winter than in summer. This emphasizes the significant KE source within the mixed layer
235 that is present in the 1/30° simulation.

236 Figure 9 shows the spectra of the buoyancy fluxes within the mixed layer:

$$237 \quad PK = \frac{1}{MLD} \int_0^{-MLD} \langle w'b' \rangle_{xy} dz \quad (1),$$

238 in the 1/30° simulation. Note that the PK spectrum is different from the co-spectrum of w' and
239 b' integrated over the ML used for a spectral energy budget analysis (e.g. Capet et al., 2008c).
240 Since this paper does not focus on the spectral energy budget, we chose the PK spectrum that
241 is much easier to compute. In the KET, STCC and STEP regions, the winter spectra peaks are
242 close to 25-40 km. These wavelengths at submesoscale match the estimation displayed on
243 Figures 1. These results suggest that the winter buoyancy flux, mostly positive within the
244 mixed-layer (Fig. 8), has the spectral peak at submesoscale in the high EKE regions.

245 Figures 10 displays the spectra of winter and summer W within the ML. The 1/30°
246 simulation highlights small energetic wavelengths at submesoscale in winter. In the KET,
247 STCC and STEP regions, winter spectral peaks (Figure 10a,c,e) are close to 25-40 km, which
248 are similar to those in the PK spectra (Figure 9a,b,c). These results suggest that the large
249 vertical motions at small scales are generate by the buoyancy fluxes within the mixed-layer in
250 winter. This confirms that winter MLI is the main mechanism that triggers submesoscales
251 leading to a seasonal RV variation and to a restratification of the mixed-layer. However, in
252 the 1/10° simulation winter and summer W spectral peaks have scales close to or larger than

253 100 km in the KET and STEP regions. In the STCC region the spectral peak emerges at 50
254 km in winter and 200 km in summer. This is consistent with the length scale of the Charney
255 instability invoked in Qiu (1999) and Qiu et al. (2008).

256 At depths below the mixed-layer, a spectral analysis of W in the $1/30^\circ$ simulation
257 (not shown) indicates steeper slopes and peaks at larger scales (> 100 km) both in winter and
258 summer with the magnitude larger in winter than in summer. These results are consistent with
259 the vertical sections of the buoyancy flux $\langle w'b' \rangle_{xy}$ as a function of time (Figures 8). The
260 buoyancy flux is mostly positive and strongly intensified within the mixed-layer with a larger
261 magnitude in winter than in summer. This further emphasizes the significant KE source
262 within the mixed-layer driving submesoscale motions that is present in the $1/30^\circ$ simulation.

263 Spectral KE fluxes (see Capet et al. 2008c, Klein et al. 2008, Sasaki and Klein 2012
264 for their equations (2) and (3)) (Figures 11) and EKE time series (Figures 5) allow to
265 characterize how the KE generated at submesoscale is transferred to other scales through the
266 non-linear interactions (S14, Q14). The spectral KE fluxes in Figures 11a-c reveal a net KE
267 transfer to larger scales starting at 25 km. This transfer is characterized by a strong seasonality,
268 in terms of amplitude and width, with a winter intensification due to the impact of
269 submesoscales. In the three regions, magnitude of the net upscale KE transfer increases from
270 25 km up to 150-200 km and then decreases. The corresponding KE fluxes vary by a factor 2
271 to 3 between the KET region and the two other regions. In order to characterize the time scale
272 of this KE transfer, we next analyze the impact of this transfer on the KE using the same
273 methodology as in S14: KE is partitioned into four wavebands: the 10-100 km, 100-200km,
274 200-300km and 300-1000km wavebands. Comparison of the KE time series in the $1/30^\circ$ and
275 $1/10^\circ$ simulations (Figures 5) reveals that presence of submesoscales leads, in all regions, to a

276 significant EKE increase for all scales smaller than 300 km. The increase factor is 1.8, 1.8 and
277 2.7 respectively for the KET, STCC and STEP regions, which agrees with Figure 4c. These
278 three regions exhibit in the $1/30^\circ$ simulation a strong EKE seasonality (with seasonal
279 amplitudes relatively to the mean value close to one) for scales up to 300 km. Without
280 submesoscale impact ($1/10^\circ$ simulation), both, the mean value and seasonal amplitude of EKE
281 are much smaller (Figures 5). One interesting characteristic is that the EKE maximum for
282 each waveband occurs with a lag of about one month compared with the time series for
283 smaller scales (maximum is approximately attained in March, April and May, respectively for
284 the 0-100km, 100-200 km and 200-300 km wavebands). These lags actually correspond to the
285 time it takes for the KE to be transferred for one waveband to the next one through the inverse
286 KE cascade (as displayed for the three regions in Figures 11a-c, see also Vallis 2006). All
287 these diagnoses suggest that winter MLI is the main mechanism leading to a significant KE
288 seasonality for scales smaller than 300 km.

289 Scales larger than 300 km contain not only large eddies but also large-scale
290 evolving currents such as meanders. Comparison between the two simulations reveals an EKE
291 increase in the $1/30^\circ$ simulation in this waveband smaller than in others (Figure 5). The
292 largest increase is in the subtropics: STCC (factor 2) and STEP (factor 1.6) (Figures 5c-f).
293 This increase factor is only 1.2 in the KET region (Figures 5a,b). As a result, although EKE in
294 this waveband well dominates other wavebands in the $1/10^\circ$ simulation, its contribution to the
295 total EKE in the $1/30^\circ$ simulation is much reduced. In terms of time variability, a significant
296 EKE seasonality for these large scales is observed only in the two subtropical regions in the
297 both simulations with the peak amplitude being in August-September (Figures 5c-f). Thus,
298 the larger production of submesoscale KE in the $1/30^\circ$ simulation appears to impact largest

299 scales in both subtropical regions through the spectral KE fluxes. This result is consistent with
300 Chen et al. (2014) indicating that eddy-mean flow interactions are “local” in subtropical gyres.
301 In the KET region (Figures 5a,b), although a more significant time variability of the EKE for
302 scales larger than 300 km is observed in the 1/30° simulation, no clear seasonality emerges
303 contrary to other wavebands. Other mechanisms, such as EKE fluxes to or from other regions
304 may explain the EKE characteristics in this waveband. These mechanisms are invoked by
305 Chen et al. (2014) for the KET, which they refer to as “non-local” processes.

306

307 **5. Impacts of submesoscales in regions with lower EKE**

308 In the three other regions (MLEP, SAEP, and SAWP), the most unstable MLI
309 wavelengths are still larger than 20-30 km in winter (Figure 1). However, the diagnostic
310 analyses in this section indicate that the MLI impact on the ocean dynamics in winter is much
311 weaker than in high EKE regions.

312 The MLEP region is however the one that most resembles the high EKE regions. It
313 experiences a RV seasonality in the 1/30° simulation with a seasonal amplitude varying with
314 a factor between 1.5 and 2 between winter and summer and with however smaller magnitudes
315 (Figure 6d) than in the first three regions with higher EKE (Figures 6a-c). The vertical
316 velocity (W) time series exhibits a similar seasonality with a factor 2-3 amplitude and is in
317 phase with the MLD time series. The meridional section of W in winter in the eastern North
318 Pacific Ocean also illustrates the larger magnitude but also the smaller scales in the MLEP
319 region (30-42°N) in the 1/30° simulation (Figure 7c) compared to the 1/10° simulation
320 (Figure 7d). Again, there is a phase lag of about one month between RV and MLD times
321 series (Figure 6d), suggesting that MLD drives MLIs and therefore the production of

322 submesoscales. Not surprisingly, without submesoscales ($1/10^\circ$ simulation), RV and W time
323 series display a much weaker seasonality. The differences between the winter MLD in the two
324 simulations emphasize the submesoscale impact on the restratification of the mixed-layer. But
325 this restratification is much weaker than in the high EKE regions (Figures 6a-c) (less than
326 10%).

327 Characteristics of these time series in winter, in particular their phase relationship
328 (see S14) suggest winter MLIs are still active. To confirm the MLI impact, we again analyze
329 the buoyancy flux (PK) spectra, that represents transformation of PE into KE within the
330 mixed-layer. From Figure 9d, there are now two winter spectral peaks in the $1/30^\circ$ simulation,
331 at 100 km and at 20 km (instead of one around 25-40 km in high EKE regions (Figures 9a-c)).
332 The resultant vertical motion W also displays the two peaks at the same scales (Figure 10g).
333 However, the $1/10^\circ$ simulation displays just one winter spectral PK peak at 100 km (Figure
334 10h). Figure 8d confirms the strong seasonality of the transformation of PE into KE with a
335 positive sign. Spectral KE fluxes on Figure 11d reveal a net KE transfer to larger scales
336 starting at 20 km. But magnitudes of these fluxes in this lower KE region is, not surprisingly,
337 more than three to four times smaller than in high EKE regions (Figures 11a-c). This suggests,
338 in the MLEP region in winter, a competition between MLIs that produce submesoscales and
339 instabilities at 100 km that produce mesoscale eddies.

340 On the other hand, MLIs in the subarctic regions (SAWP and SAEP), although still
341 well resolved in the $1/30^\circ$ simulation (Figure 1), are no more the dominant process explaining
342 submesoscales. Figures 9e,f and Figures 10i,k emphasize that the wavelength of buoyancy
343 flux and large vertical motions within the mixed layer in these regions is ~ 100 km in winter
344 and summer. Time series of the RV and MLD rms values, and in particular their phase lags,

345 also suggest MLIs do not dominate the dynamics in winter (Figures 6e,f). The RV rms values
346 are still much larger in the 1/30° simulation than in the 1/10° simulation, with a non-
347 negligible seasonality, but there is no systematic phase lag with the RV and MLD time series
348 (as it should occur when MLIs is the main mechanism producing submesoscales, see Q14,
349 S14). Furthermore, there is no restratification in the 1/30° simulation, and on the contrary, the
350 winter MLD is larger in this simulation compared to the 1/10° one (Figures 6e,f). Since this
351 restratification process is known to be mostly triggered by energetic frontal submesoscales,
352 this means that submesoscales are either, not energetic enough, or have not a strong frontal
353 character (density fronts at small-scale are not strong enough). This non-frontal character is
354 emphasized by the vertical section of the buoyancy fluxes (Figures 8e,f) that are negative
355 (down-gradient) at the mixed-layer base during the fall. Spectral KE fluxes in the subarctic
356 regions (Figures 11e,f) further emphasize the impact of instabilities at 100 km: there is a net
357 KE transfer to larger scales starting at 20 km, but this KE transfer is clearly intensified at 100
358 km.

359 These discrepancies, related to the MLI impact in winter, appear to agree with the
360 velocity spectrum slope in the different regions (although interpretation of these slopes is not
361 so meaningful as other diagnoses). Indeed, the velocity spectrum slope (not shown), in the
362 high EKE regions is in k^{-2} in winter and k^{-3} in summer in the 1/30° simulation. The same
363 spectrum slopes are observed in the MLEP region. But, in subarctic regions, these slopes are
364 respectively in k^{-3} in winter and $k^{-3.5}$ in summer. A classical interpretation (Pierrehumbert et
365 al. 1994; Held et al 1995; Capet et al. 2008b; Klein and Lapeyre 2009) is that a k^{-2} slope for
366 the velocity spectrum is a signature of the surface frontal character of the mesoscale and
367 submesoscale turbulence whereas a k^{-3} slope is more representative of the geostrophic

368 turbulence. Thus, although all these diagnoses do not constitute a definite proof, they suggest
369 that the winter production of submesoscales in subarctic regions may be partly explained by
370 MLIs, but is certainly mostly explained by the direct enstrophy cascade, more energetic in
371 winter because of the larger KE production at 100km.

372 To further confirm the discrepancies between subarctic regions and the MLEP
373 region, we again compare the KE time series in the 1/30° and 1/10° simulations. Figures 5g,h
374 in the MLEP region clearly reveal that KE production at submesoscale leads to increase KE in
375 the 10-100 km waveband. But there is no clear relationship between the KE time series in the
376 10-100km range with those of larger scales. The KE transfer from 20 km to these larger scales
377 (as emphasized by Figure 11d), appears to be not large enough to affect significantly larger
378 scales. These larger scales should be driven mostly by the KE production at 100 km (Figures
379 9d). On the other hand, the KE magnitude in all of the time series (except for KE scales larger
380 than 300 km) is much larger in the 1/30° simulation than in the 1/10° one (Figures 5g,h),
381 although the latter well resolves the 100 km scale. One classical explanation, usually invoked
382 in geostrophic turbulence studies (Lapeyre et al. 1999; Joseph and Legras 2002; Lapeyre
383 2002) is that using a higher numerical resolution allows to better represent the velocity shear
384 around mesoscale eddies (that acts as a dynamical barrier), which allows these eddies to be
385 more coherent for a longer time instead of being quickly dissipated.

386 In terms of KE seasonality, the MLEP region displays a strong seasonal signal in
387 the 1/30° simulation, not observed in the 1/10° simulation. But this is observed only for scales
388 smaller than 200 km (black curve on Figure 5g). Again, contribution of MLIs mostly explains
389 this seasonality in this waveband with a peak in April (principally KE for scales smaller than
390 100 km: see purple curve on Figure 5g). A similar seasonality is observed for scales smaller

391 than 200 km in subarctic regions (black curves on Figures 5i,k). But contribution of MLIs
392 (through the KE for scales smaller than 100 km) is too small to explain this signal (purple
393 curves on Figures 5i,k). Furthermore, in the SAEP region the KE peak (black curve on
394 Figures 5k) occurs in different months, either in April (in 2002) or in August (in 2003). The
395 instability at 100 km is a strong candidate to explain this seasonality. But a better
396 understanding of the dynamics in these subarctic regions requires first to better identify the
397 mechanisms (and their potential seasonality) that force these instabilities at 100 km in the
398 upper oceanic layers.

399

400 **6 Discussion**

401 This study focuses on the impact of scales between 16 km and 50 km (we call
402 submesoscales) on the dynamics in the North Pacific Ocean. This is done through the
403 comparison of two numerical simulations, identical except for the numerical resolution
404 (respectively $1/30^\circ$ and $1/10^\circ$, allowing to resolve physical wavelengths about 5 times the grid
405 spacing). Thus, one simulation takes into account submesoscales, the other does not. Results
406 indicate that submesoscale impact leads in all regions, not only to an increase of the KE by a
407 factor up to 3, but also to a significant seasonality of this KE. These KE changes can be
408 mostly explained by the MLIs within the upper oceanic layer in winter and the subsequent KE
409 transfer to larger scale, which are however geographically dependent. In high KE regions, KE
410 production is strongly intensified within the mixed-layer in winter and mostly explained by
411 MLIs that produce KE with large vertical motions at submesoscale within the upper oceanic
412 layers, whereas the KE production is low with vertical motions at scales close to 100 km in
413 summer. The resulting winter submesoscale KE is subsequently transferred to larger scales

414 leading to a seasonal EKE evolution with a maximum in spring or summer. Thus, surface
415 frontal dynamics at small scales appears to be the dominant mechanism explaining the strong
416 KE increase and its seasonality. In regions with lower KE, in particular in subarctic regions,
417 the surface frontal dynamics such MLI is no more the main mechanism explaining the KE
418 changes. Indeed, KE production is also intensified in winter but is mostly dominated year-
419 around by instabilities at scales close to 100 km. Furthermore, the winter mixed-layer is
420 deepening instead of shallowing when submesoscales are taken into account. Since both
421 simulations resolve well scales of the order of 100 km, it is suggested that the significant KE
422 increase due to submesoscales in the lower KE regions can be explained using arguments of
423 geostrophic turbulence, and in particular in terms of dynamical barriers (intensified at
424 submesoscales) around mesoscale eddies that prevent these eddies to be dissipated too
425 quickly.

426 All these results need however to be checked more carefully, which is the focus of a
427 future study. First the type of instabilities that occur in the different regions at scales close to
428 100 km needs to be determined. The baroclinic instability of large-scale vertical current
429 shears in the upper oceanic layers with a wavelength of the order of 100 km, corresponding to
430 Charney-type instability, seems to be the most relevant one as reported in Qiu (1999) and
431 Capet et al. (2016). This mechanism may be a candidate to explain the large-scale seasonality
432 in lower EKE regions. But what causes these large-scale instabilities in the different regions
433 should be carefully investigated. Furthermore, the present results do not rule out that MLIs
434 (although having scales well resolved in the $1/30^\circ$ simulation) are more energetic in the lower
435 KE regions than found in our study. Indeed, a higher resolution may lead to surface density
436 fronts more intensified and therefore more likely to be affected by MLI. Production of

437 submesoscales in the upper oceanic layers is also driven by other mechanisms such as small-
438 scale frontogenesis, wind induced frontal instabilities occurring at smaller scales. Thus, the
439 surface frontal dynamics at small scales may be more energetic in these regions (see
440 Thompson et al. 2016) but the geostrophic turbulent character is likely to still be the dominant
441 one.

442 The relative impact of these different mechanisms, surface frontal dynamics at
443 small-scale and geostrophic turbulence driven by large-scale instabilities, needs also to be
444 better quantified than is done in the present study. An energy budget that mixes the
445 approaches followed by Roulet et al. (2012) and Chen et al. (2016) would be a suitable
446 methodology. The simulations used in the present study are well appropriate to follow this
447 methodology.

448

449 **Acknowledgements**

450 The simulations were performed on the Earth Simulator under support of JAMSTEC. H.S.
451 is supported by CANON Foundation. P.K. acknowledges the support of IFREMER (through
452 the MOU IFREMER-JAMSTEC), CNRS (France) and the Agence Nationale pour la
453 Recherche [Contract ANR-10-LABX-19-01 (LabexMER)]. B.Q. acknowledges Science Team
454 support from NASA's SWOT mission NNX16AH66G. We appreciate comments from two
455 reviewers, that significantly improved the manuscript.
456

457 **References**

- 458 Boccaletti G, Ferrari R, Fox-Kemper B (2007) Mixed layer instabilities and restratification. *J Phys*
459 *Oceanogr* 37(9): 2228–2250.
- 460 Buckingham CE, Naveira Garabato AC, Thompson AF, Brannigan L, Lazar A, Marshall DP, George
461 Nurser AJ, Damerell G, Heywood KJ, Belcher SE (2016) Seasonality of submesoscale flows in the
462 ocean surface boundary layer. *Geophys Res Lett* 43(5): 2118–2126.
- 463 Callies J, Ferrari R, Klymak JM, Gula J (2015) Seasonality in submesoscale turbulence. *Nat Commun*
464 6:6862. doi: 10.1038/ncomms7862
- 465 Callies J, Flierl G, Ferrari R, Fox-Kemper B (2016) The role of mixed-layer instabilities in
466 submesoscale turbulence. *J Fluid Mech* 788: 5–41.
- 467 Capet X, Campos E J, Paiva M (2008a) Submesoscale activity over the Argentinian shelf. *Geophys*
468 *Res Lett* 35: 2–6.
- 469 Capet X, Klein P, Hua BL, Lapeyre G, McWilliams JC (2008b) Surface kinetic energy transfer in
470 surface quasi-geostrophic flows. *J fluid mech* 604: 165–174.
- 471 Capet X, McWilliams JC, Molemaker MJ, Shchepetkin AF (2008c) Mesoscale to Submesoscale
472 Transition in the California Current System. Part III: Energy Balance and Flux. *J Phys Oceanogr*
473 38(10): 2256–2269.
- 474 Capet X, Rouillet G, Klein P, Maze G. (2016) Intensification of upper-ocean submesoscale turbulence
475 through Charney baroclinic instability. *J Phys Oceanogr* 46(11): 3365–3384.
- 476 Chen R, Flierl GR, Wunsch C (2014) A description of local and nonlocal eddy–mean flow interaction
477 in a global eddy-permitting state estimate. *J Phys Oceanogr* 44(9): 2336–2352.
- 478 Chen R, Thompson AF, Flierl GR (2016) Time-dependent eddy-mean energy diagrams and their
479 application to the ocean. *J Phys Oceanogr* 46(9): 2827–2850,

480 de Boyer Montégut C, Madec G, Fischer AS, Lazar A, Iudicone D (2004) Mixed layer depth over the
481 global ocean: An examination of profile data and a profile-based climatology. *J Geophys Res* 109:
482 C12003.

483 Dufau C, Orszynowicz M, Dibarboure G, Morrow R, Le Traon PY (2016) Mesoscale resolution
484 capability of altimetry: Present and future, *J Geophys Res Oceans* 121(7): 4910–4927

485 Ferrari R, Wunsch C (2009) Ocean circulation kinetic energy: reservoirs, sources and sinks. *Ann Rev*
486 *Fluid Mech* 41(1): 253–282.

487 Fox-Kemper B, Ferrari R, Hallberg R (2008) Parameterization of mixed layer eddies. Part I: theory
488 and diagnosis. *J Phys Oceanogr* 38(6): 1145–1165.

489 Haines T, Marshall JC (1998), Gravitational, symmetric and baroclinic instability of the ocean mixed-
490 layer. *J Phys Oceanogr* 28(4): 634–658.

491 Hakim GJ, Snyder C, Muraki DJ (2002) A new surface model for cyclone–anticyclone asymmetry. *J*
492 *Atmos Sci* 59 (16): 2405–2420.

493 Hanawa K, Talley LD (2001) Mode waters, in *Ocean circulation and climate: observing and*
494 *modelling the global ocean*, edited by G. Siedler, J. Church, and J. Gould, pp. 373–386, Academic,
495 San Diego, Calif.

496 Hautala SL, Roemmich DH (1998) Subtropical mode water in the Northeast Pacific Basin. *J Geophys*
497 *Res Oceans* 103(C6): 13055–13066.

498 Haza AC, Ozgökmen TM, Griffa A, Garaffo ZD, Piterbarg L (2012) Parameterization of particle
499 transport at submesoscales in the Gulf Stream region using Lagrangian subgridscale models.
500 *Ocean Modell* 42: 31–49.

501 Held IM, Pierrehumbert RT, Garner ST, Swanson KL (1995) Surface Quasigeostrophic Dynamics. *J*
502 *Fluid Mechan* 282: 1–20.

503 Joseph B, Legras B (2002) Relation between kinematic boundaries, stirring and barriers for the
504 Antarctic polar vortex. *J Atmos Sci*, 59, 1198–1212.

505 Klein P, Hua BL, Lapeyre G, Capet X, Le Gentil S, Sasaki H (2008) Upper ocean turbulence from
506 high-resolution 3D simulations. *J Phys Oceanogr*, 38: 1748-1763.

507 Klein P, Lapeyre G (2009) The oceanic vertical pump induced by mesoscale and submesoscale
508 turbulence. *Annu Rev Mar Sci* 1 : 351–375.

509 Komori N, Takahashi K, Komine K, Motoi T, Zhang X, Sagawa G (2005) Description of sea-ice
510 component of coupled ocean sea-ice model for the earth simulator (oifes). *J Earth Simulator* 4: 31–
511 45.

512 Lapeyre G (2002) Characterization of finite-time Lyapunov exponents and vectors in two-dimensional
513 turbulence. *Chaos* 12: 688–698.

514 Lapeyre G, Klein P, Hua BL (1999) Does the tracer gradient vector align with the strain eigenvectors
515 in 2-D turbulence? *Phys Fluids* 11: 3729–3737.

516 Lapeyre G, Klein P, Hua BL (2006) Oceanic restratification forced by surface frontogenesis. *J Phys*
517 *Oceanogr* 36(8): 1577–1590.

518 Lévy M, Ferrari R, Franks PJS, Martin AP, Rivière P (2012a) Bringing physics to life at the
519 submesoscale. *Geophys Res Lett* 39(14): L14602. doi:10.1029/2012GL052756.

520 Lévy M, Resplandy L, Klein P, Capet X, Iovino D, Éthé C (2012b) Grid degradation of submesoscale
521 resolving ocean models: Benefits for offline passive tracer transport. *Ocean Modelling* 48: 1–9.

522 Masumoto Y, et al. (2004) A fifty-year eddy-resolving simulation of the World Ocean: Preliminary
523 outcomes of OFES (OGCM for the Earth Simulator). *J Earth Simulator* 1: 35–56.

524 McWilliams JC (2016) Submesoscale currents in the ocean. *Proc R Soc A* (472): 20160117.

525 McWilliams JC, Colas F, Molemaker MJ (2009) Cold filamentary intensification and oceanic surface
526 convergence lines. *Geophys Res Lett* 36: 1–5.

527 Mensa JA, Garraffo Z, Griffa A, Özgökmen TM, Haza A, Veneziani M (2013) Seasonality of the
528 submesoscale dynamics in the Gulf Stream region. *Ocean Dyn* 63: 923–941.

529 Nakamura N (1988) Scale selection of baroclinic instability - Effects of stratification and
530 nongeostrophy. *J Atmos Sci* 45(21): 3253–3268.

531 Noh Y, Kim HJ (1999) Simulations of temperature and turbulence structure of the oceanic boundary
532 layer with the improved near-surface process. *J Geophys Res Oceans* 104(C7): 15621–15634.

533 Nonaka M, Sasai Y, Sasaki H, Taguchi B, Nakamura H (2016) How potentially predictable are
534 midlatitude ocean currents? *Scientific Reports* 6: 20153. doi: 10.1038/srep20153

535 Onogi K, et al. (2007) The jra-25 reanalysis. *J Met Soc Jap* 85(3): 369–432.

536 Pacanowski RC, Griffies SM (1999) The MOM 3 Manual, GFDL Ocean Group Tech. Rep. 4, 680 pp.,
537 NOAA/Geophys Fluid Dyn Lab, Princeton, N. J.

538 Pierrehumbert RT, Held IM, Swanson KL (1994) Spectra of local and non-local two-dimensional
539 turbulence. *Chaos* 4: 1111–1116.

540 Qiu B (1999) Seasonal eddy field modulation of the North Pacific Subtropical Countercurrent:
541 TOPEX/POSEIDON observations and theory. *J Phys Oceanogr* 29(10): 2471–2486.

542 Qiu B, Scott R, Chen S (2008) Length scales of eddy generation and nonlinear evolution of the
543 seasonally-modulated South Pacific Subtropical Countercurrent. *J Phys Oceanogr* 38(7): 1515–
544 1528.

545 Qiu B, Chen S, Klein P, Sasaki H, Sasai Y (2014) Seasonal mesoscale and submesoscale eddy
546 variability along the North Pacific Subtropical Countercurrent. *J Phys Oceanogr* 44(12): 3079–
547 3098.

548 Roullet G, McWilliams JC, Capet X, Molemaker MJ (2012) Properties of steady geostrophic
549 turbulence with isopycnal outcropping. *J Phys Oceanogr* 42(1): 18–38.

550 Sasaki H., Klein P (2012) SSH wavenumber spectra in the North Pacific from a high-resolution
551 realistic simulation. *J Phys Oceanogr* 42(7): 1233–1241.

552 Sasaki H, Klein P, Qiu B, Sasai Y (2014) Impact of oceanic scale-interactions on the seasonal
553 modulation of ocean dynamics by the atmosphere. *Nat Commun* 5: 5636.
554 doi:10.1038/ncomms6636.

555 Stone PH (1966) On non-geostrophic baroclinic instability. *J Atmos Sci* 23: 3253–3268.

556 Suga T, Motoki K, Aoki Y, Macdonald AM (2004) The North Pacific climatology of winter mixed
557 layer and mode waters. *J Phys Oceanogr* 34(1): 3–22.

558 Thompson AF, Lazar A, Buckingham C, Naveira Garabato AC, Damerell GM, Heywood KJ (2016)
559 Open-ocean submesoscale motions: A full seasonal cycle of mixed layer instabilities from gliders.
560 *J Phys Oceanogr* 46(4): 1285–1307.

561 Tulloch R, Marshall J, Hill C (2011) Scales, growth rates and spectral fluxes of baroclinic instability
562 in the ocean. *J Phys Oceanogr* 41(6): 1057–1076.

563 Vallis GK (2006) *Atmospheric and Oceanic Fluid Dynamics*. Cambridge University Press, 745 pp.

564 Zhai X, Greatbatch RJ, Kohlmann JD (2008) On the seasonal variability of eddy kinetic energy in the
565 Gulf Stream region. *Geophys Res Lett* 35(24): L24609. doi: 10.1029/2008GL036412.

566 Zhong Y, Bracco A (2013) Submesoscale impacts on horizontal and vertical transport in the Gulf of
567 Mexico. *J Geophys Res* 118(10): 5651–5668.

568

569 **Figure captions**

570 Figure 1. Unstable MLI wavelength (km) ($2\pi L$, $L^2=N^2h^2(1+Ri)/f^2$ where N , h , Ri , and f are
571 the buoyancy frequency, MLD, Richardson number and Coriolis frequency respectively). (a)
572 December, (b) January, and (c) February in 2002.

573

574 Figure 2. Surface relative vorticity ($1e-5 s^{-1}$) estimated from velocities on (a, c) March 1 and
575 (b, d) September 1, 2002 in the (a, b) $1/30^\circ$ and (c, d) $1/10^\circ$ simulations. Analyses in this
576 study are conducted in the boxes with sub-boxes respectively: Kuroshio Extension (KET,
577 $144^\circ E-168^\circ W$ and $30-42^\circ N$), subtropical Countercurrent (STCC, $135-165^\circ E$ and $18-28^\circ N$),
578 subtropical Eastern Pacific (STEP, $150-126^\circ W$ and $15-27^\circ N$), mid-latitude Eastern Pacific
579 (MLEP, $142-130^\circ W$ and $30-42^\circ N$), subarctic Western Pacific (SAWP, $158-178^\circ E$ and $42-$
580 $52^\circ N$), and subarctic Eastern Pacific (SAEP, $165-145^\circ W$, $42-52^\circ N$) boxes shown in Fig. 2a.

581

582 Figure 3. MLD (m) in March 2002 in the (a) $1/30^\circ$ and (b) $1/10^\circ$ simulations. The MLD is
583 defined as the depth at which potential density is large by $0.03 \sigma_\theta$ from the density at surface.
584 (c) Difference of the MLD ((a) – (b)).

585

586 Figure 4. EKE ($1e-4 m^2 s^{-2}$) estimated from surface velocity anomalies from 2001 to 2003 in
587 the (a) $1/30^\circ$ and (b) $1/10^\circ$ simulations. (c) Difference of the EKEs ((a) – (b)).

588

589 Figure 5. Time series of EKE ($m^2 s^{-2}$) from 2001 to 2003 in the (a, b) KET, (c, d) STCC, (e, f)
590 STEP, (g, h) MLEP, (i, j) SAWP, and (k, l) SAEP boxes. EKE in the scale ranges of (purple)
591 < 100 km, (green) $100-200$ km, (red) $200-300$ km, (blue) > 300 km, and (orange) all length.

592 The right (left) vertical axis is the scale for the KE of all length (other scales). (a, c, e, g, i, k)
593 the 1/30° simulation and (b, d, f, h, j, l) 1/10° simulation. Note that the vertical scales in each
594 figure are different.

595

596 Figure 6. Time series of (black curve) relative vorticity rms ($1e-5 \text{ s}^{-1}$), (blue curve) vertical
597 velocity rms (10 m day^{-1}), and (red curve) MLD (m) from 2001 to 2003 in the boxes of (a)
598 KET, (b) STCC, (c) STEP, (d) MLEP, (e) SAWP, and (f) SAEP. (solid color curves) 1/30°
599 simulation and (pastel color curves) 1/10° simulation.

600

601 Figure 7. Meridional sections (from 15°N to 50°N) of the vertical velocity (m day^{-1} , in color)
602 and the potential density (σ_θ , isolines) on March 1, 2002 at (a,b) 160°E and (c,d) 135°W in
603 (a,c) the 1/30° simulation and (b,d) the 1/10° simulation.

604

605 Figure 8. Time variations of energy transformation from potential energy to kinetic energy (\langle
606 $w'b' >_{xy}$) as a function of depth in 2002 in the 1/30° simulation. (a) KET, (b) STCC, (c)
607 STEP, (d) MLEP, (e) SAWP, and (f) SAEP boxes. The color scale of 7d,e,f (from -1.5 to 1.5
608 ($1e-4 \text{ kg m}^{-3} \text{ cm s}^{-1}$)) is different from that of 7a,b,c (from -5 to 5 ($1e-4 \text{ kg m}^{-3} \text{ cm s}^{-1}$)).

609

610 Figure 9. Wavenumber spectra of buoyancy flux exhibiting energy transformation from
611 potential energy to kinetic energy within the mixed-layer (PK in the equation (1)) in (black
612 curves) winter (February and March) and (red curves) summer (from July to September) in
613 the 1/30° simulation. (a) KET, (b) STCC, (c) STEP, (d) MLEP, (e) SAWP, and (f) SAEP
614 boxes.

615

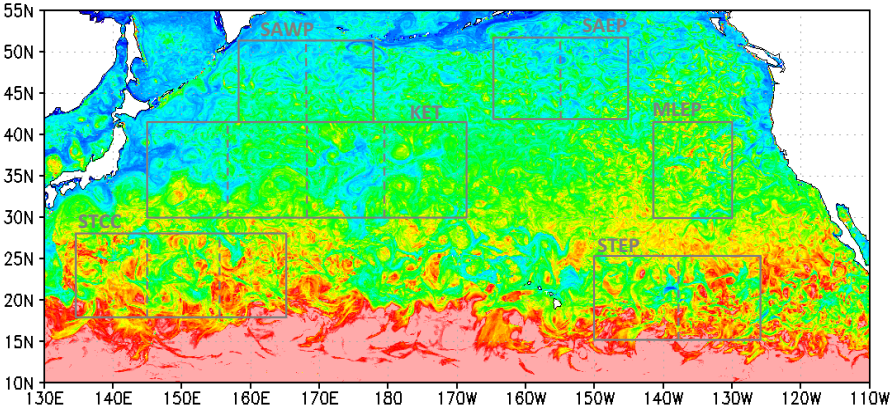
616 Figure 10. Wavenumber spectra of vertical velocity within the mixed-layer in (black curves)
617 winter (February and March) and (red curves) summer (from July to September) in the (a,b)
618 KET, (c,d) STCC, (e,f) STEP, (g,h) MLEP, (i,j) SAWP, and (k,l) SAEP boxes. (left) $1/30^\circ$
619 simulation and (right) $1/10^\circ$ simulation.

620

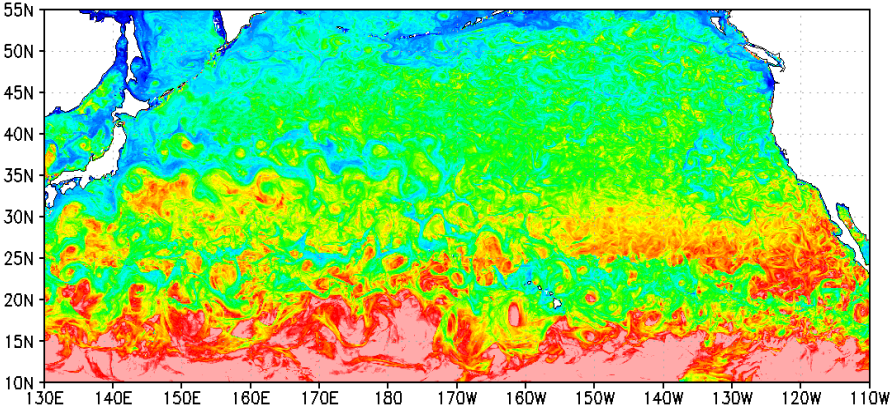
621 Figure 11. Spectral KE fluxes using geostrophic velocities in winter (black curves) and
622 summer (red curves) in the $1/30^\circ$ simulation. (a) KET, (b) STCC, (c) STEP, (d) MLEP, (e)
623 SAWP, and (f) SAEP boxes. Note that the vertical scales in each figure are different.

Figure 1

(a) $2\pi L$, Dec 2002



(b) $2\pi L$, Jan 2002



(c) $2\pi L$, Feb 2002

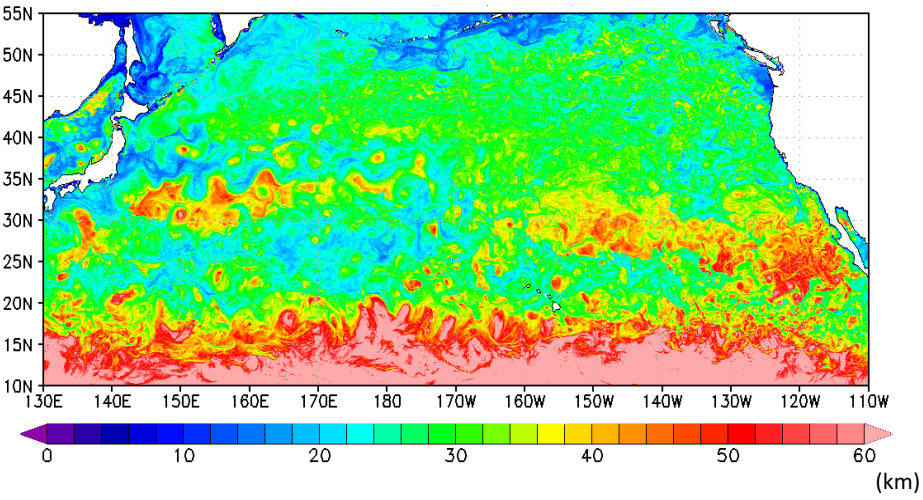


Figure 2

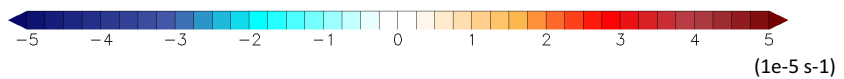
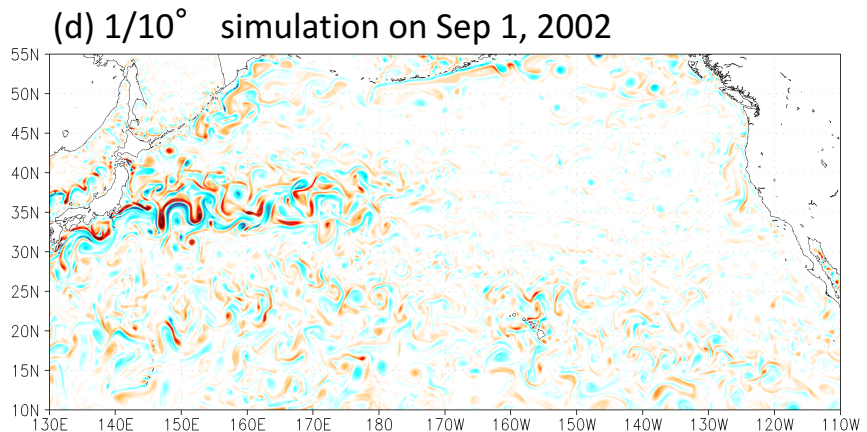
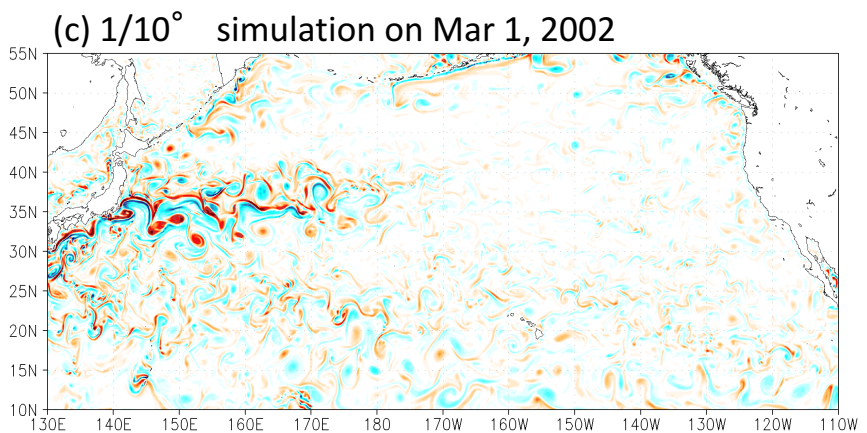
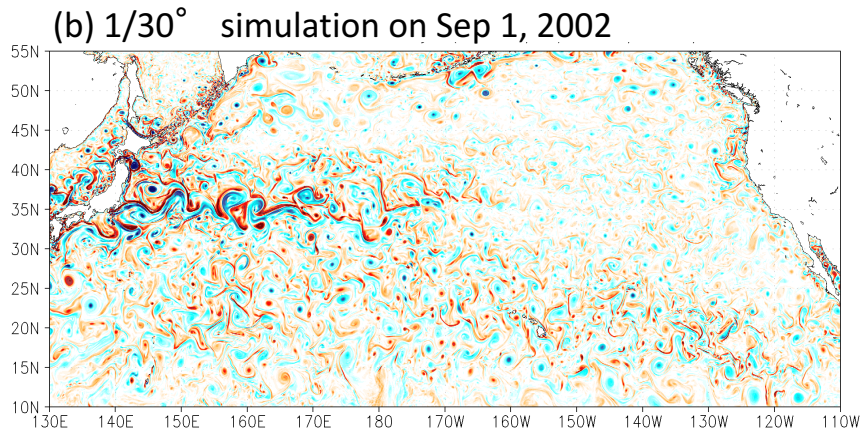
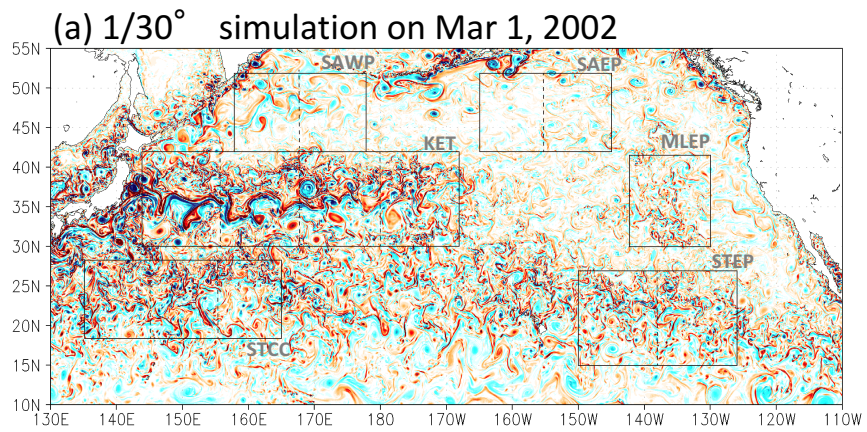
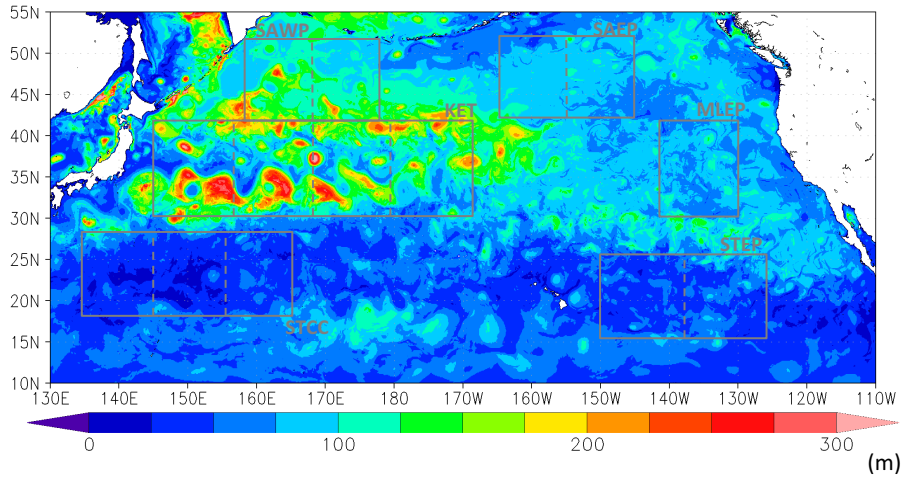
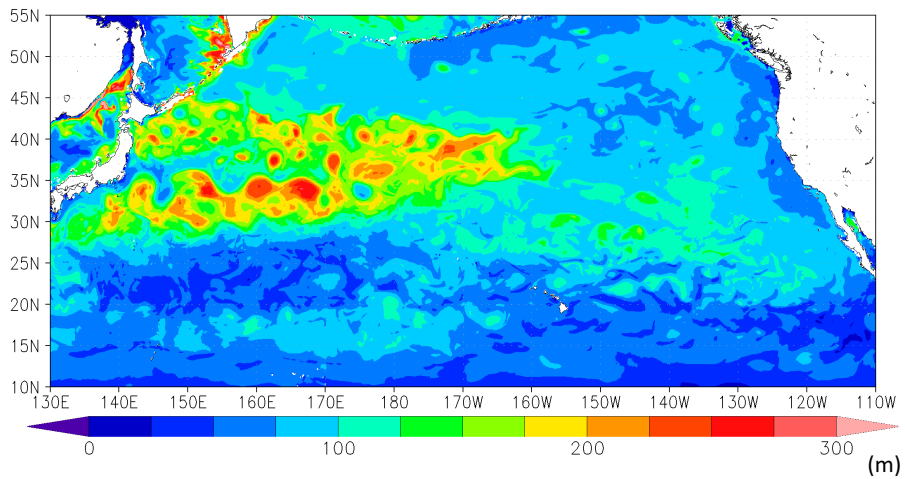


Figure 3

(a) ML depth ($1/30^\circ$, Mar 2002)



(b) ML depth ($1/10^\circ$, Mar 2002)



(c) ML depth ((a) - (b))

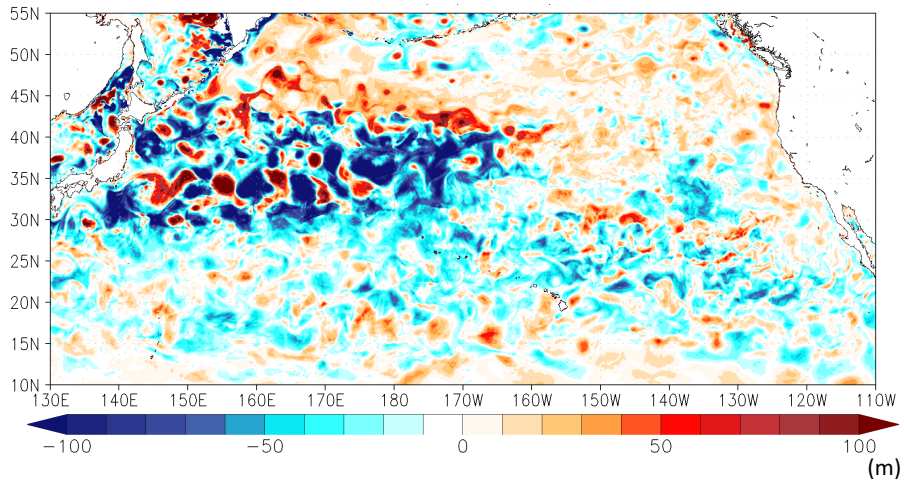


Figure 4

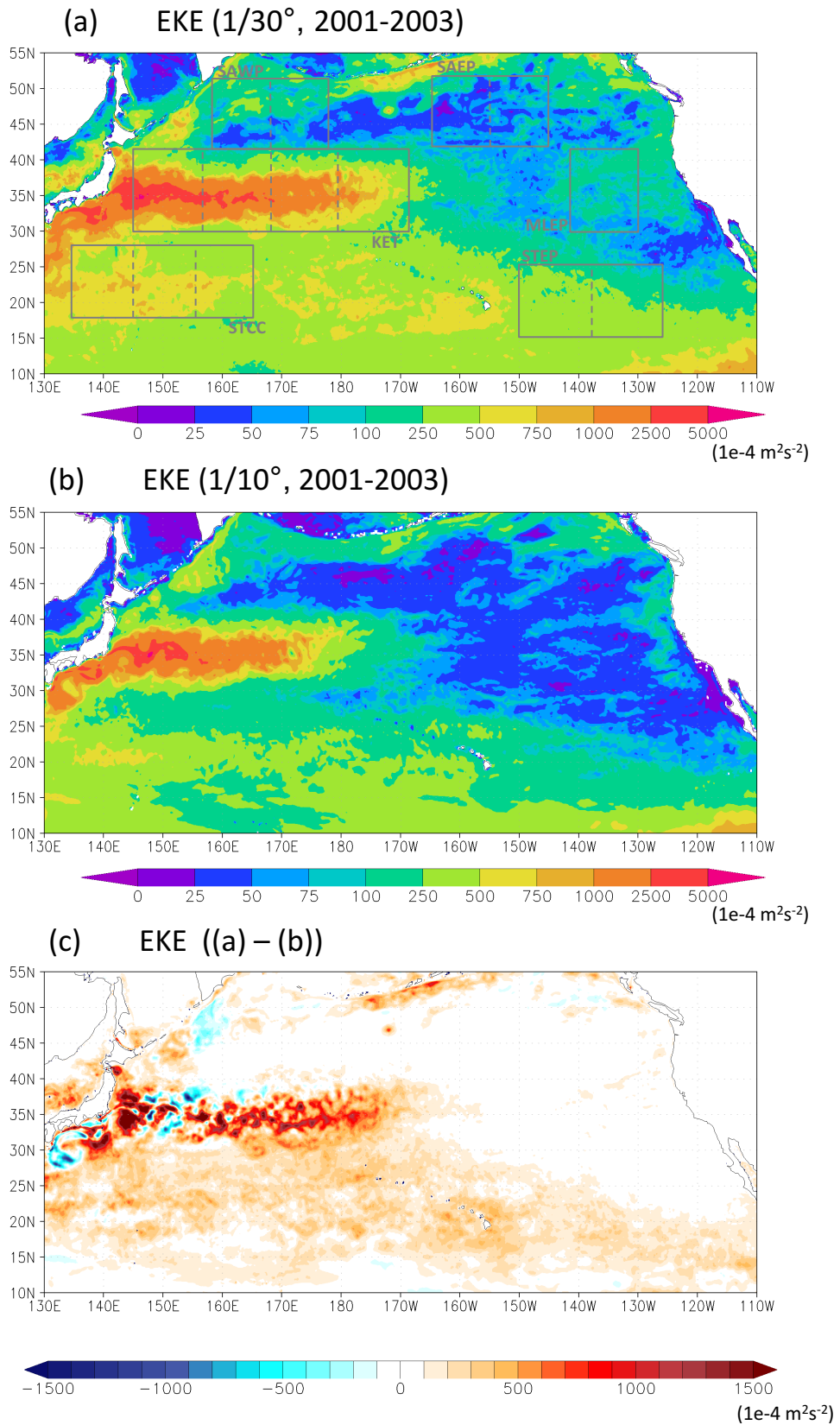
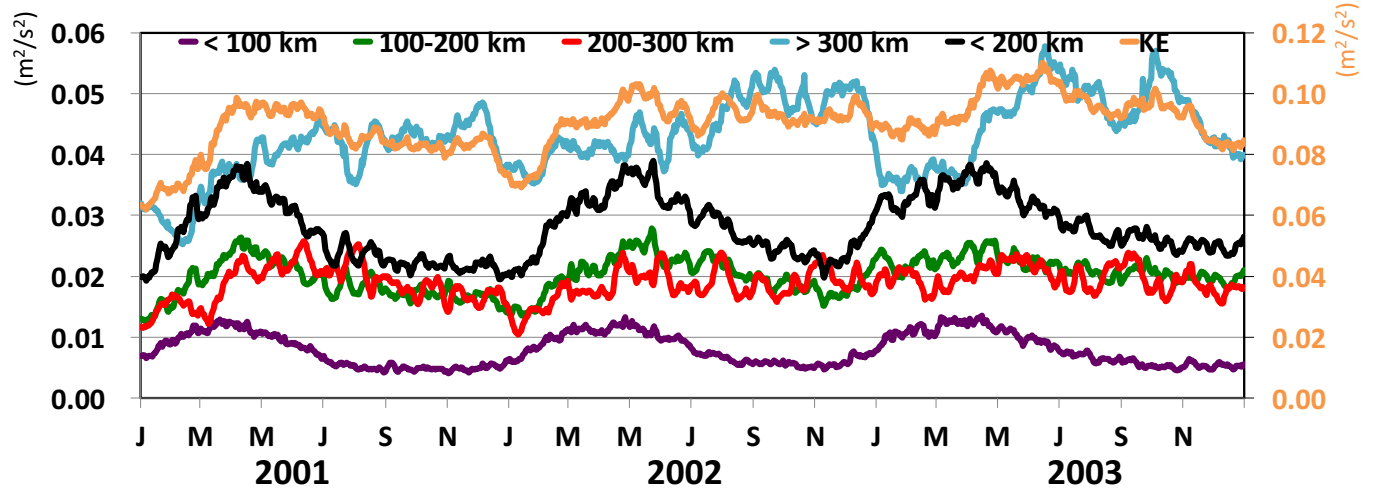


Figure 5

(a) KET BOX in the 1/30° simulation



(b) KET BOX in the 1/10° simulation

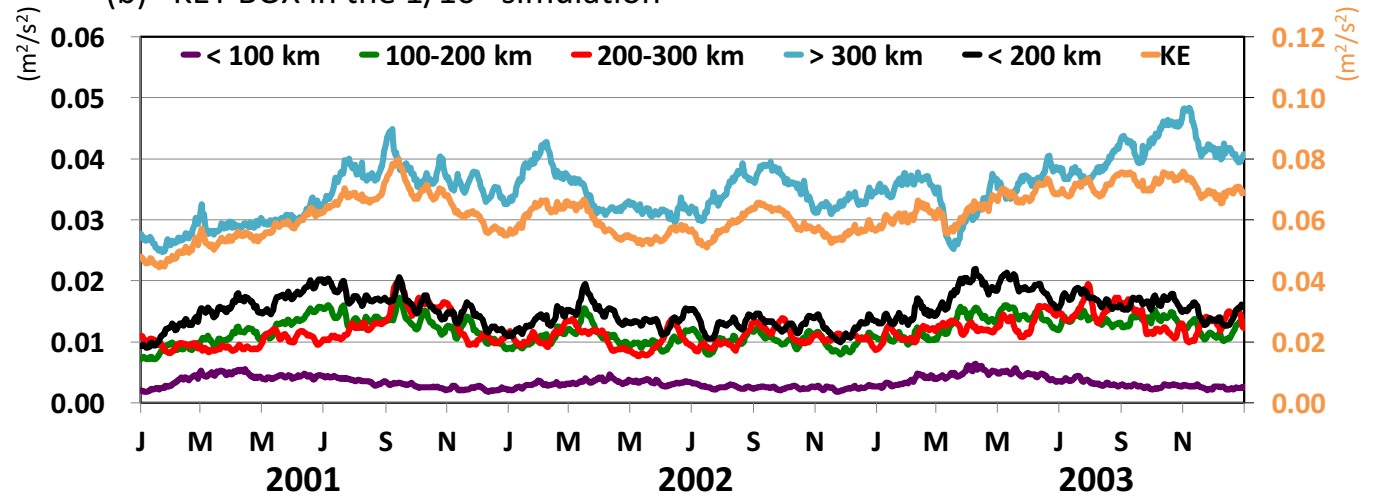
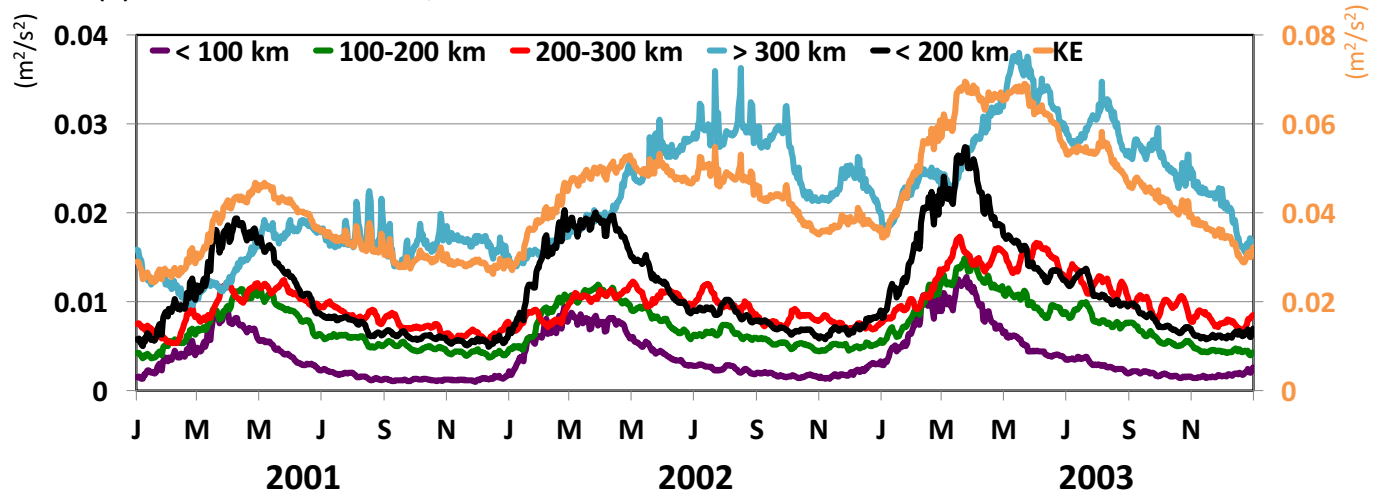


Figure 5

(c) STCC BOX in the 1/30° simulation



(d) STCC BOX in the 1/10° simulation

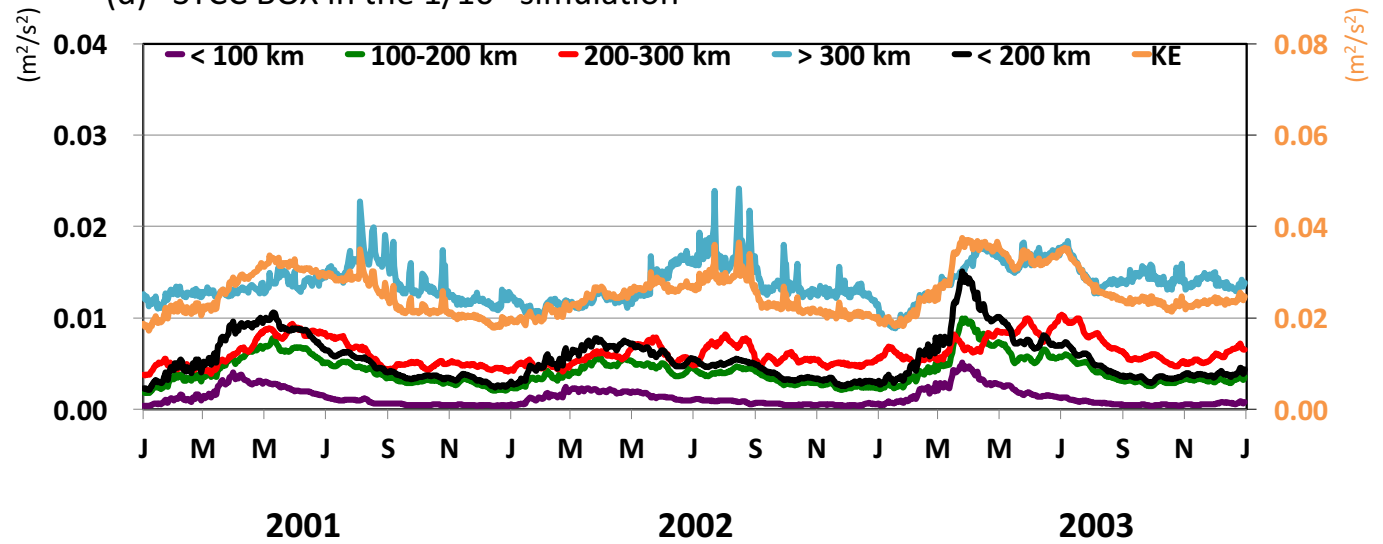
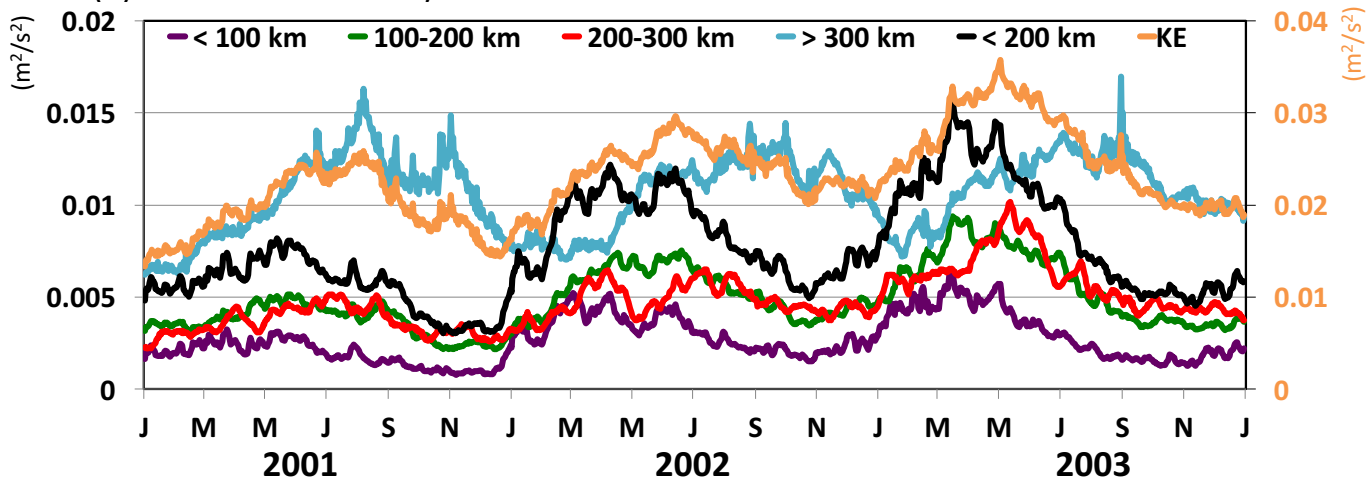


Figure 5

(e) STEP BOX in the $1/30^\circ$ simulation



(f) STEP BOX in the $1/10^\circ$ simulation

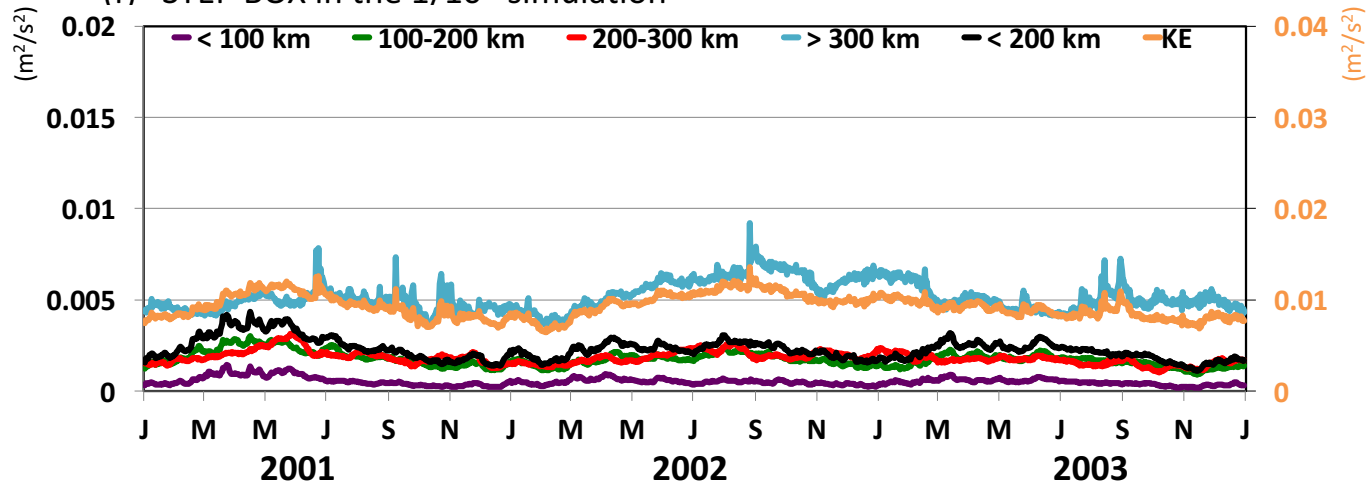
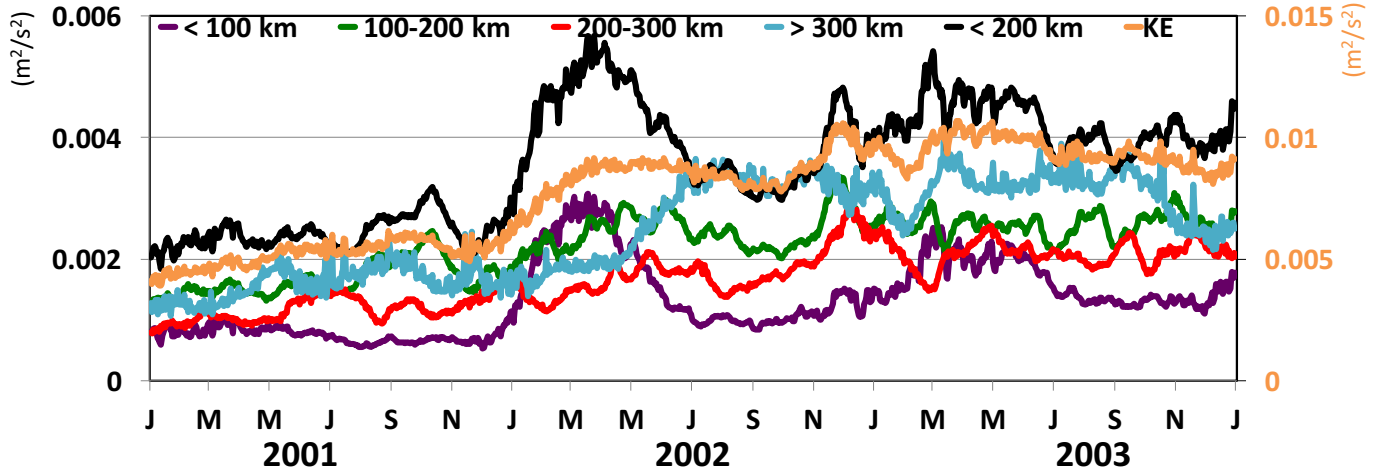


Figure 5

(g) MLEP BOX in the 1/30° simulation



(h) MLEP BOX in the 1/10° simulation

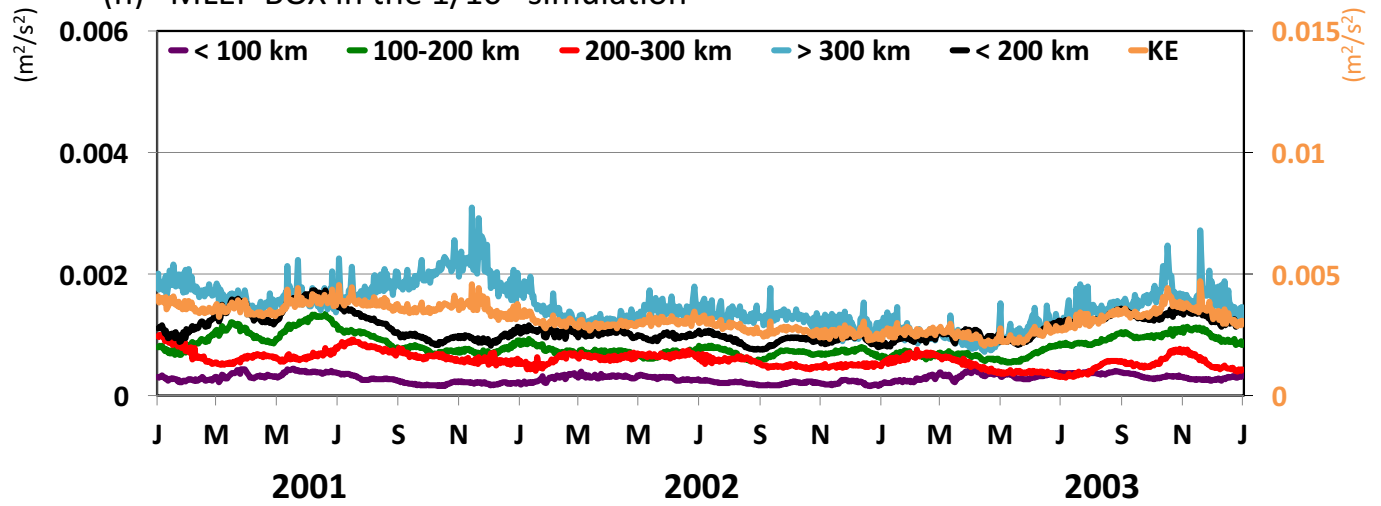
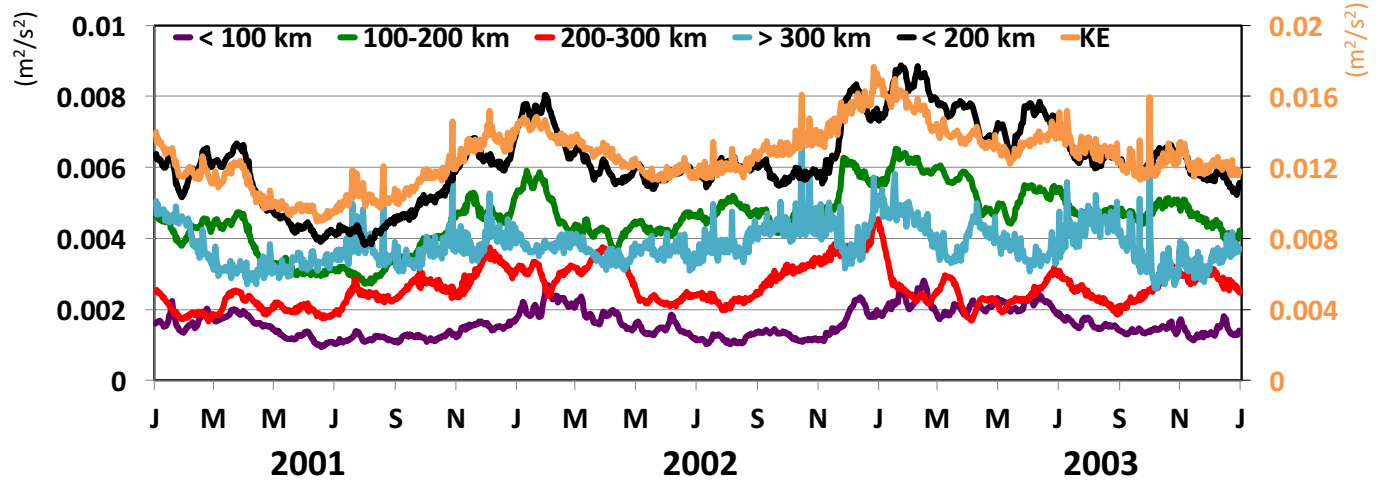


Figure 5

(i) SAWP BOX in the 1/30° simulation



(j) SAWP BOX in the 1/10° simulation

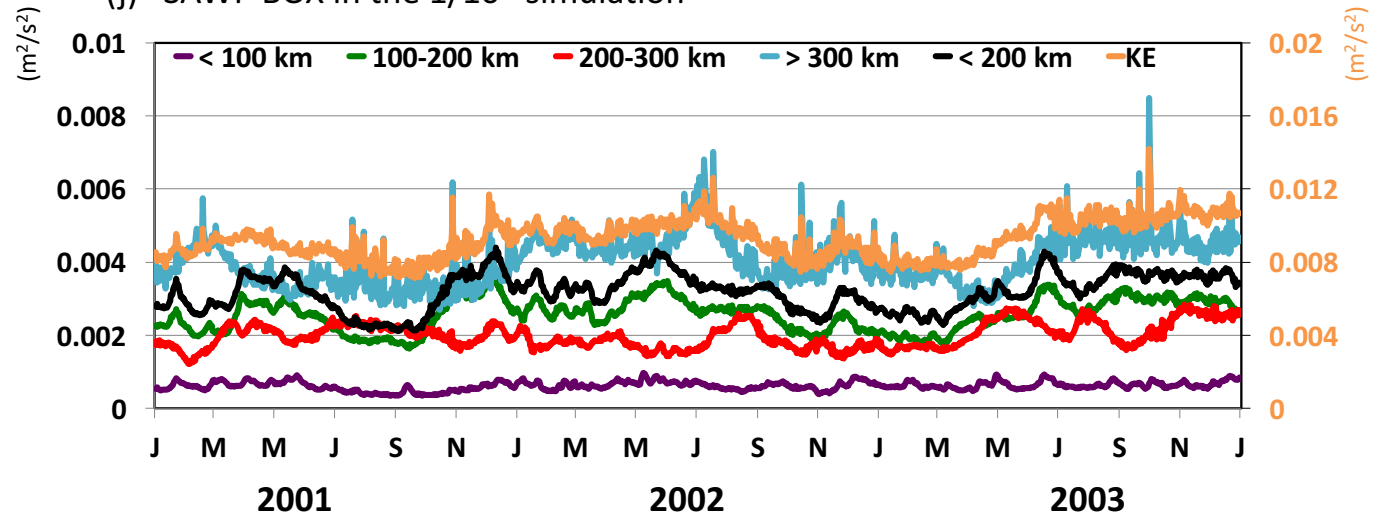
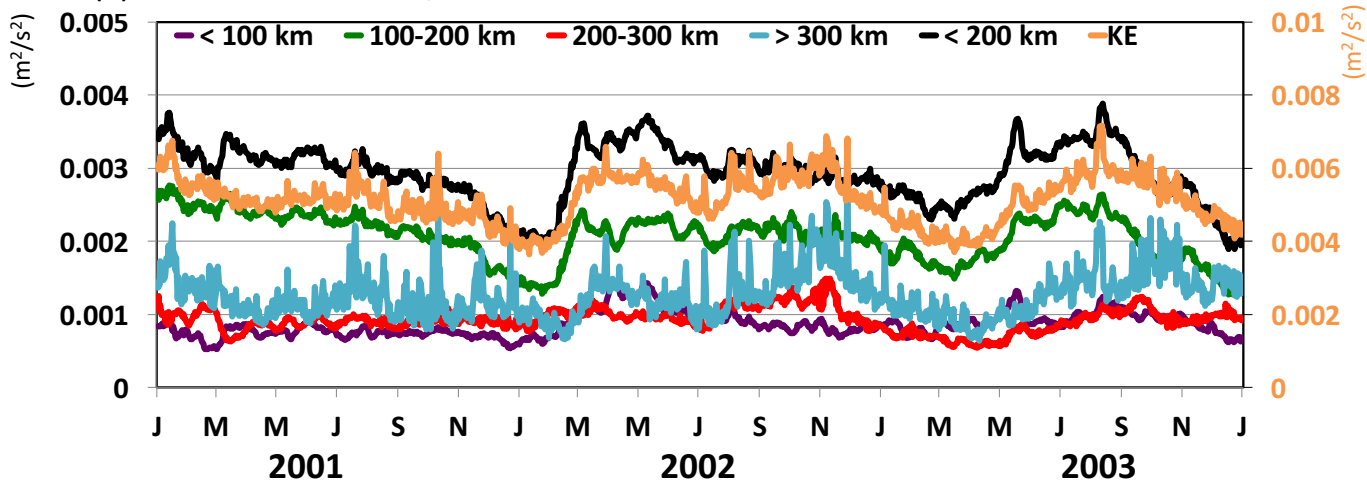


Figure 5

(k) SAEP BOX in the $1/30^\circ$ simulation



(l) SAEP BOX in the $1/10^\circ$ simulation

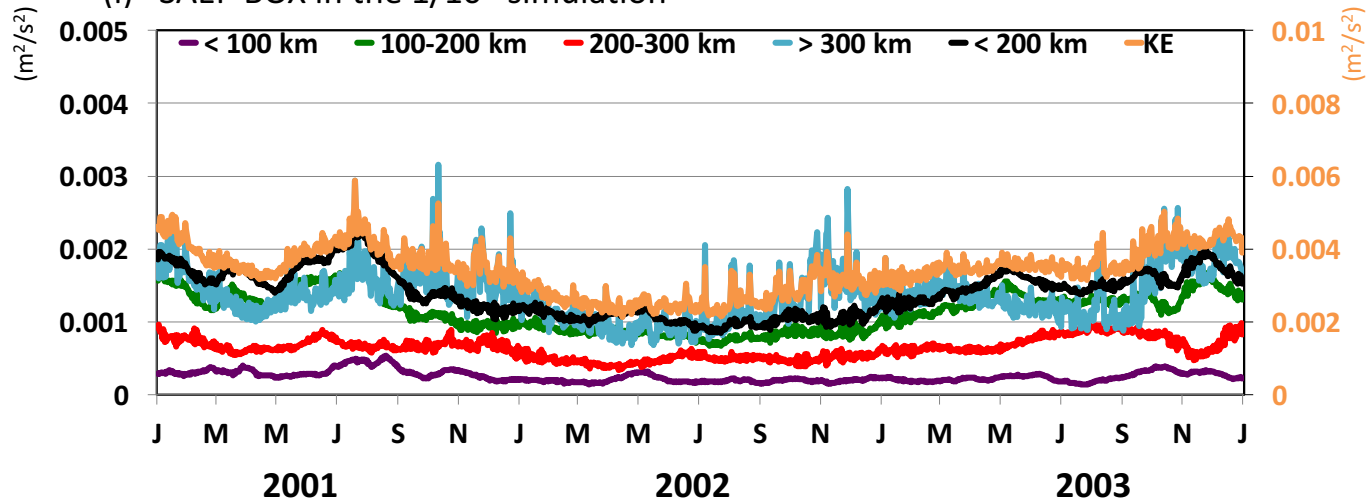


Figure 6

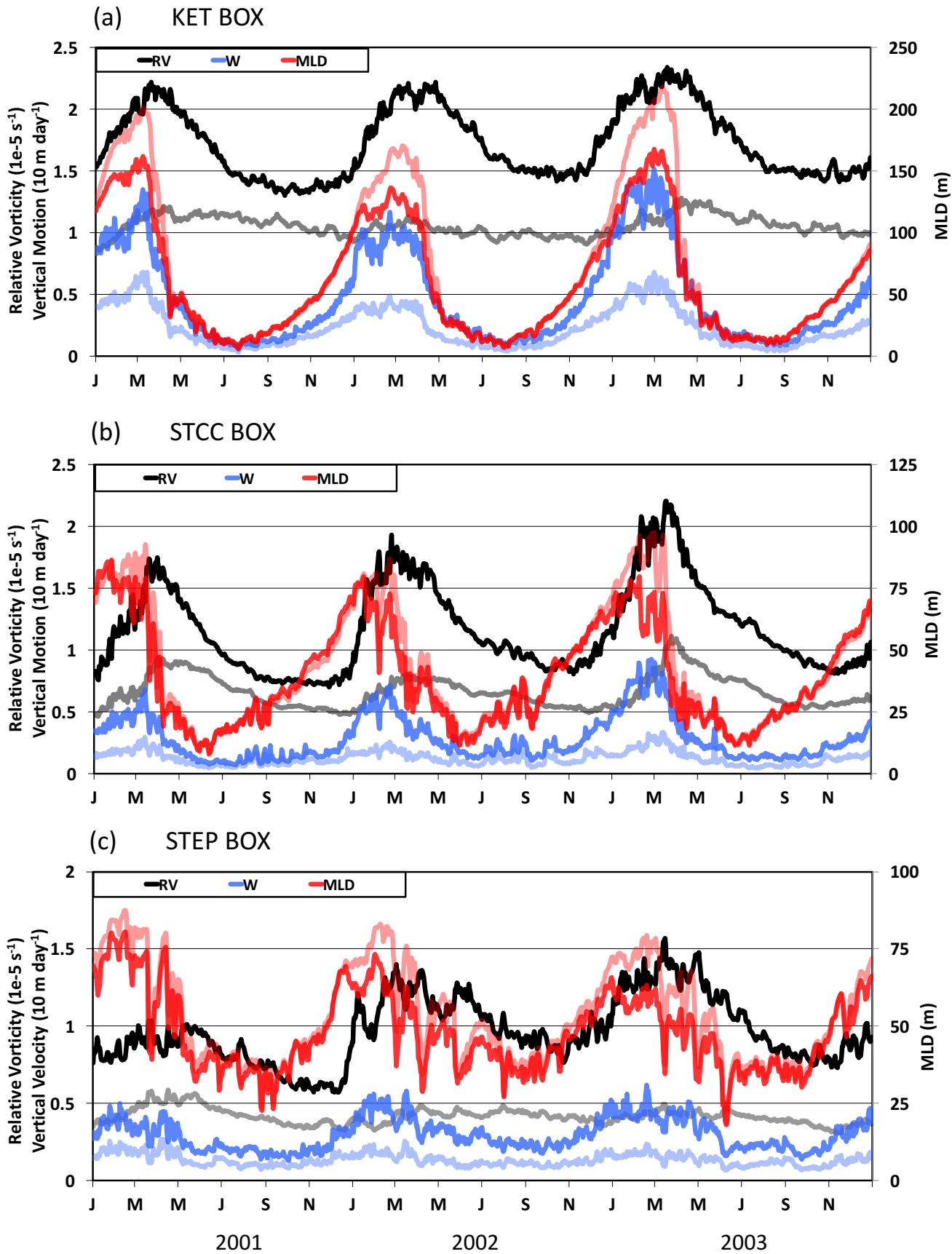


Figure 6

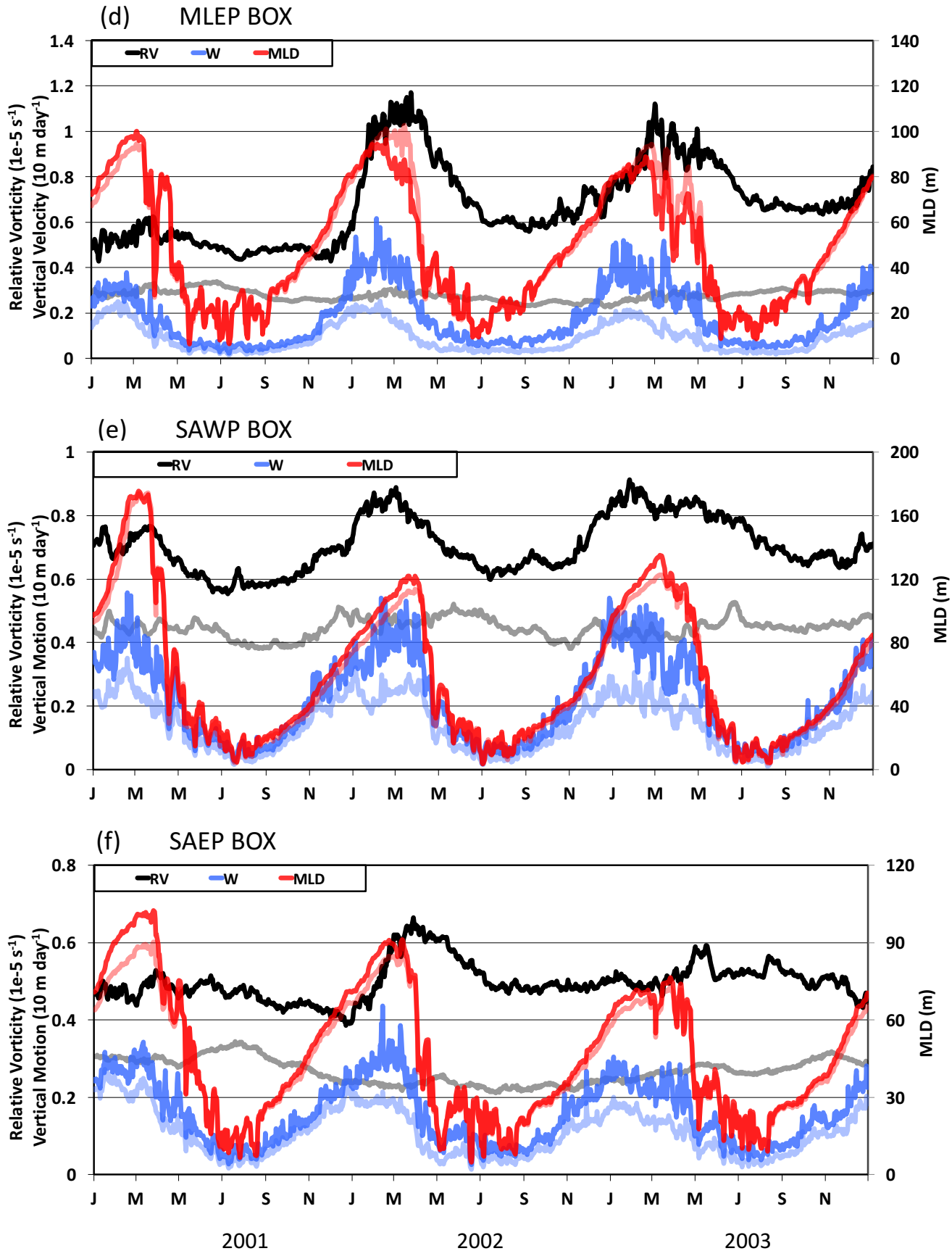


Figure 7

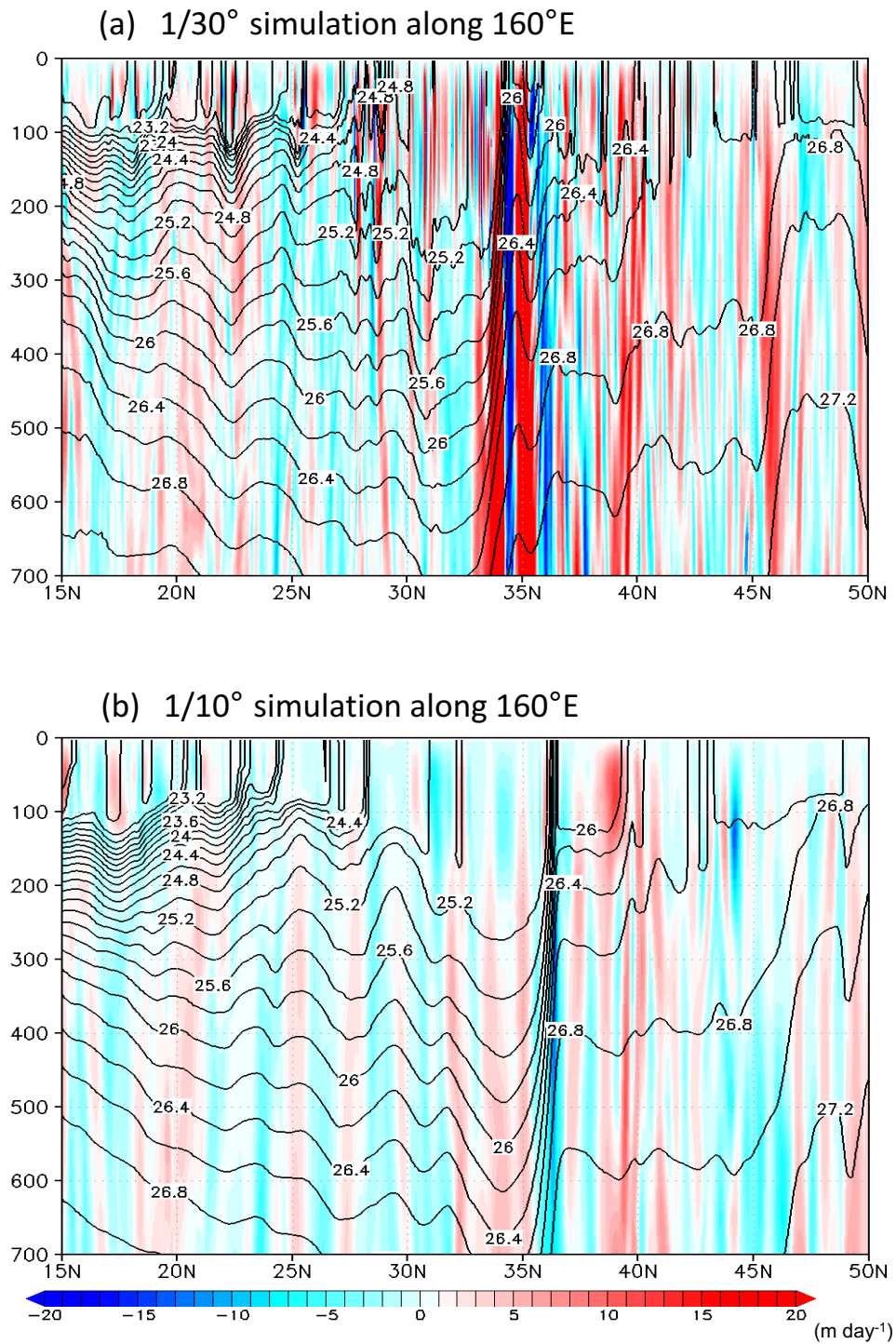


Figure 7

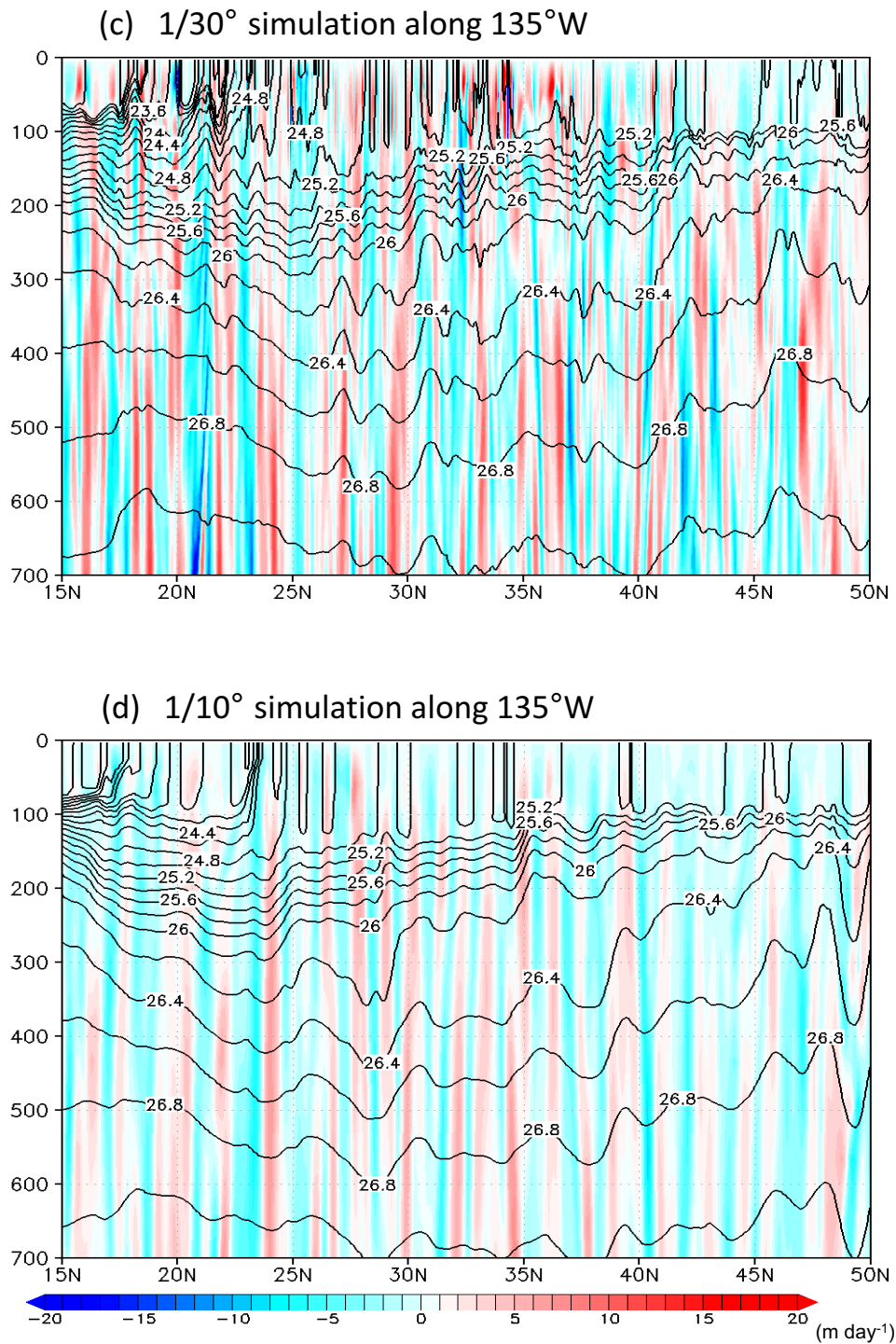


Figure 8

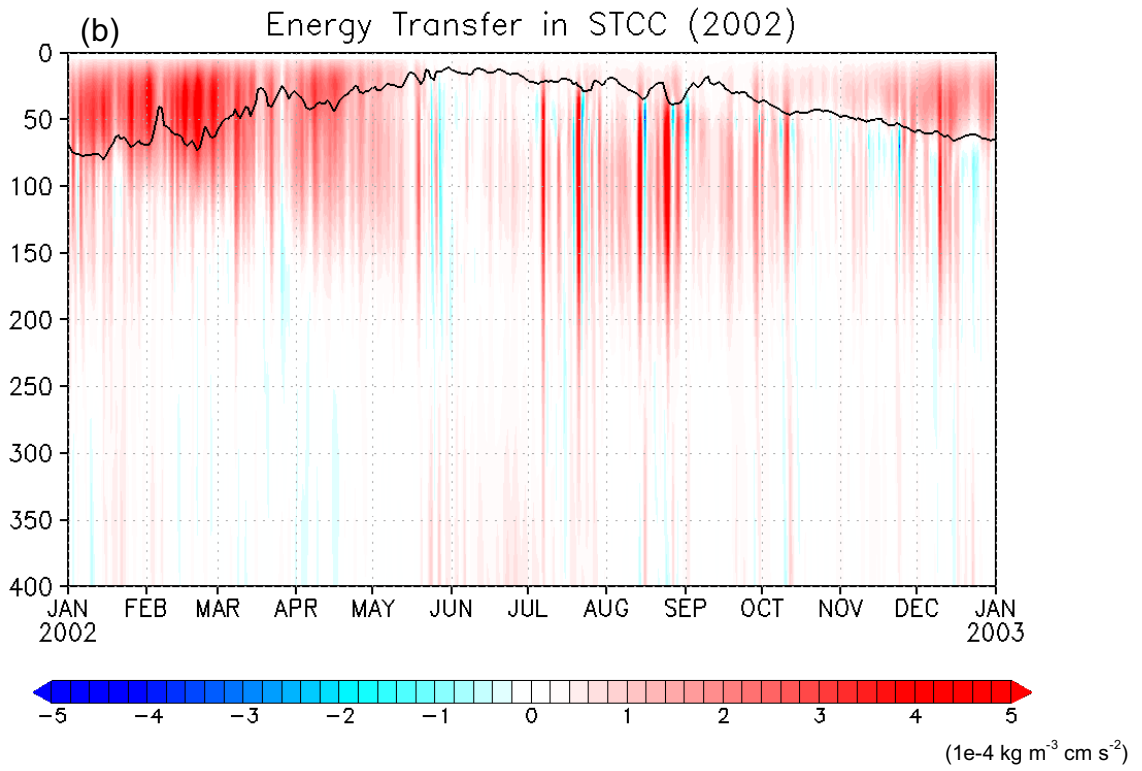
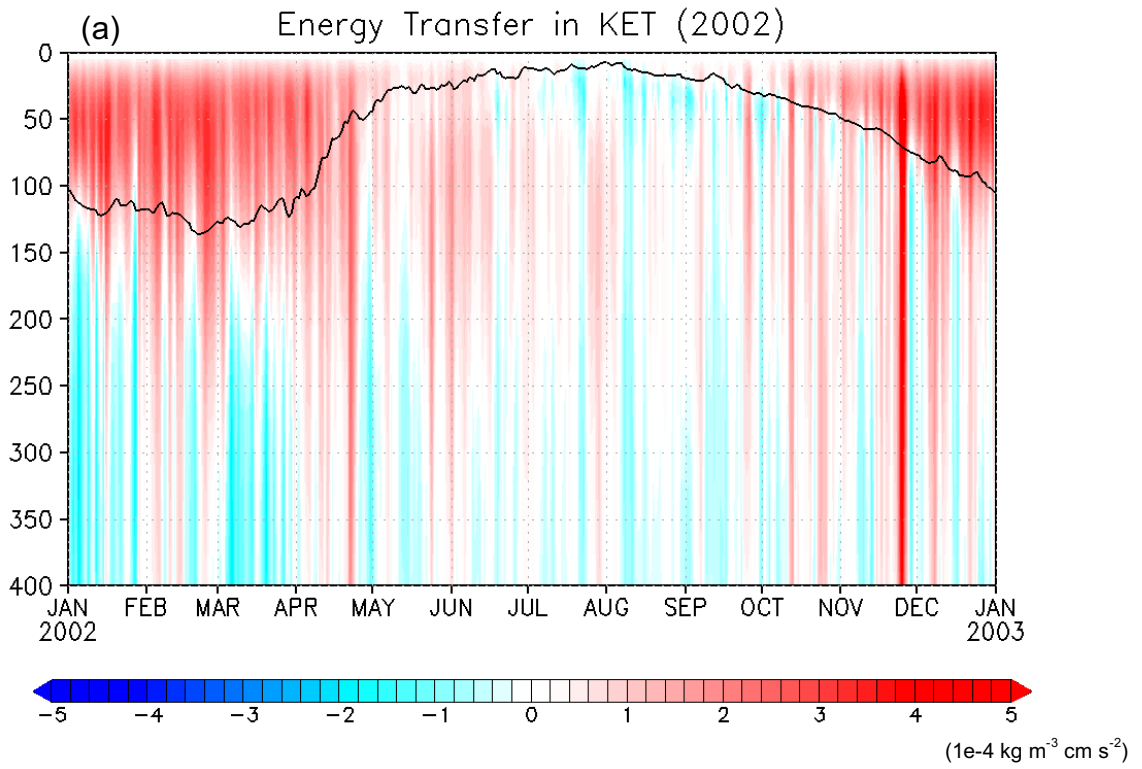


Figure 8

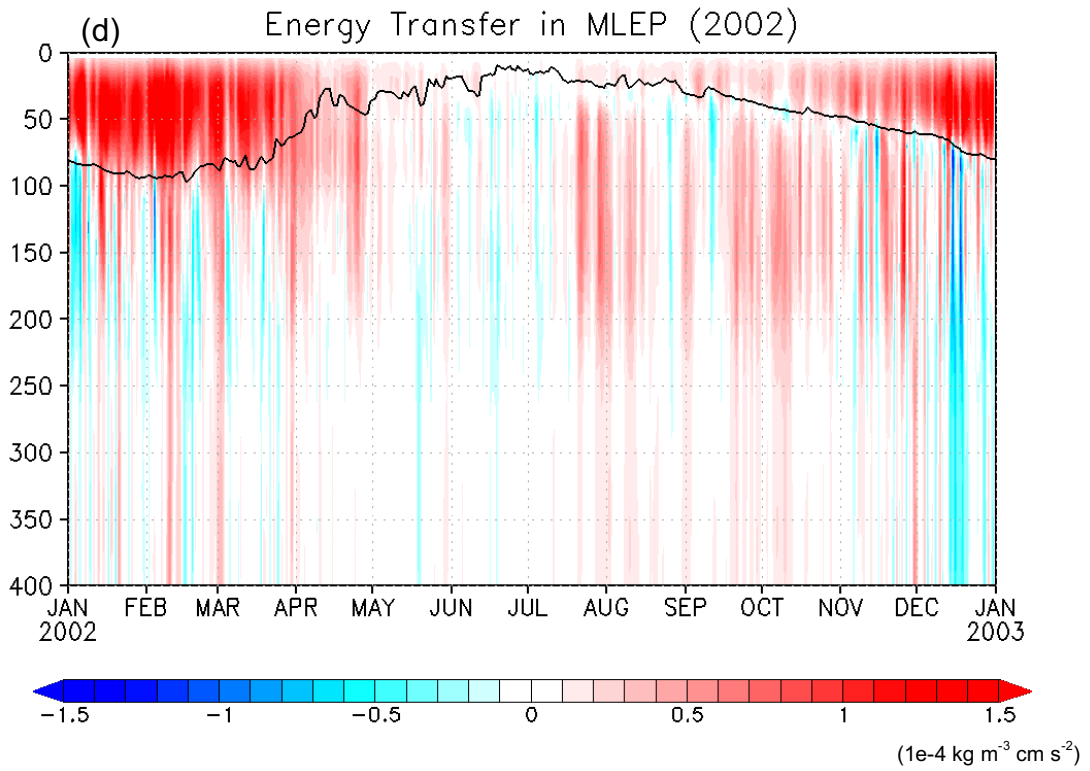
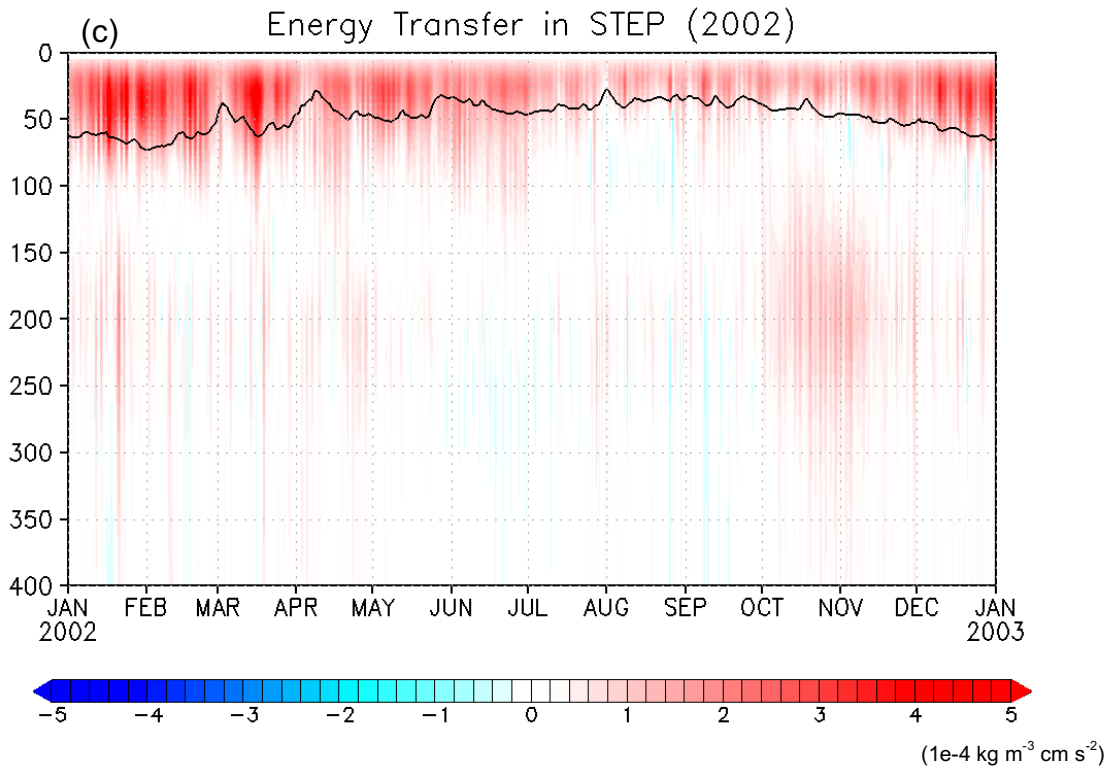


Figure 8

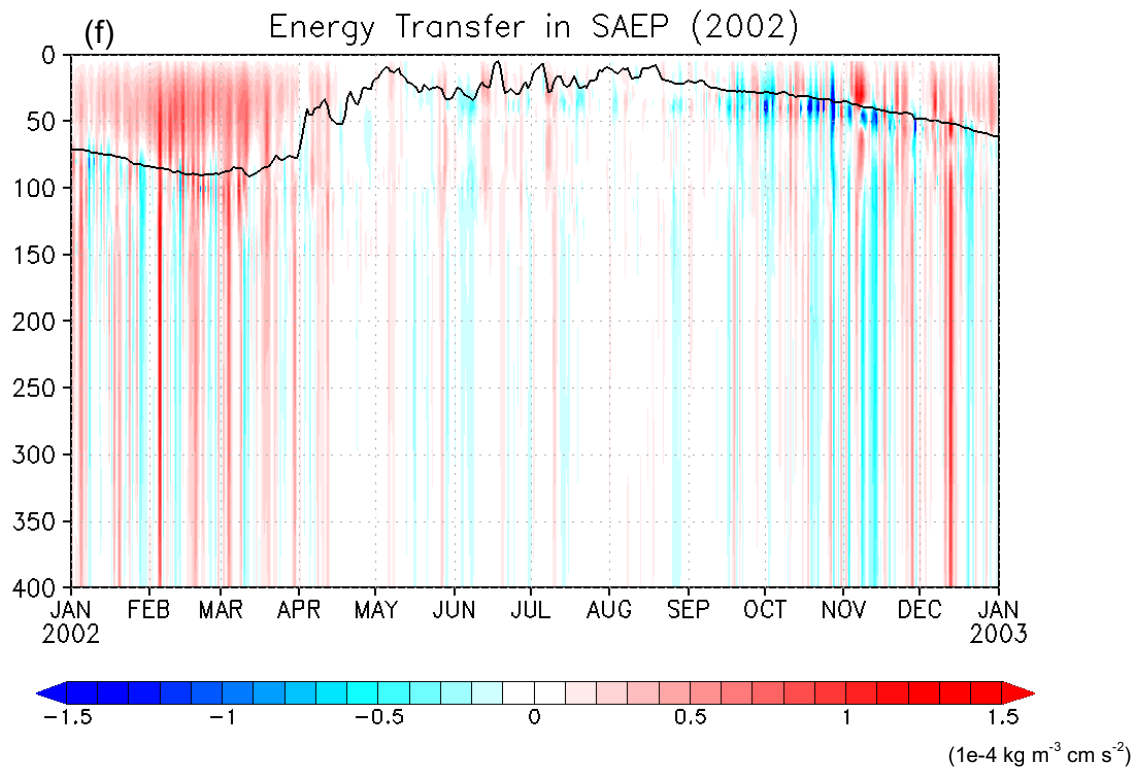
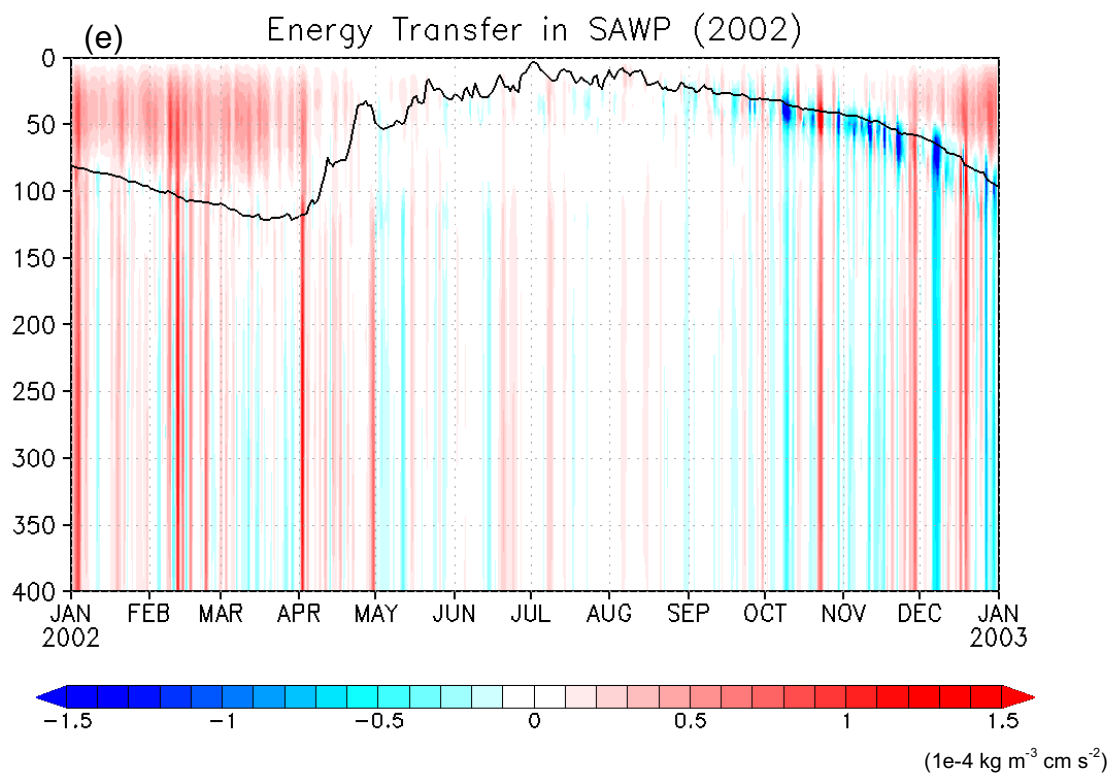
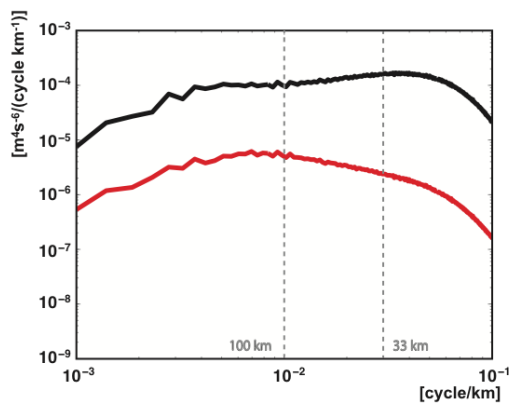
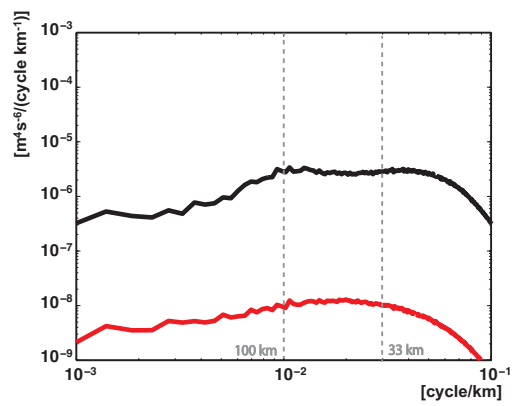


Figure 9

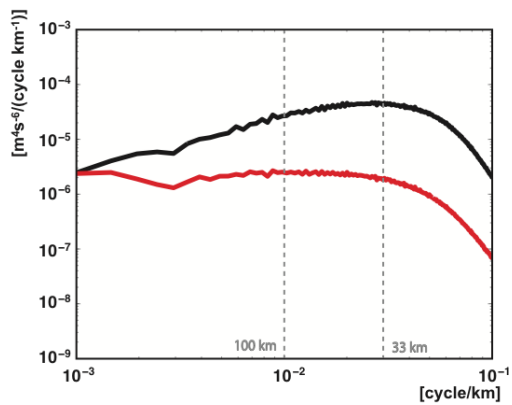
(a) KET



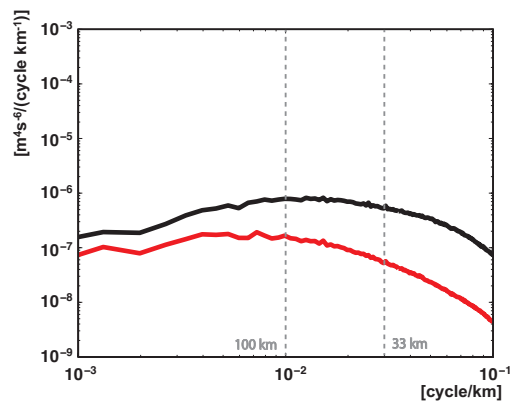
(d) MLEP



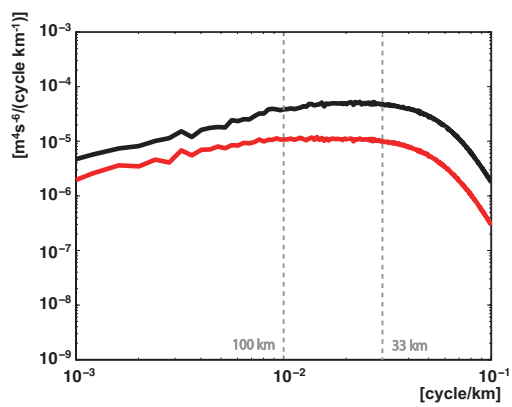
(b) STCC



(e) SAWP



(c) STEP



(f) SAEP

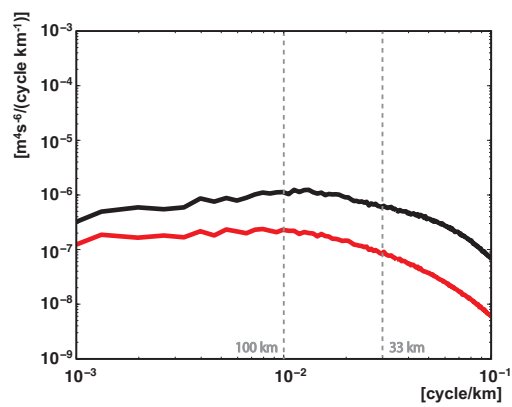
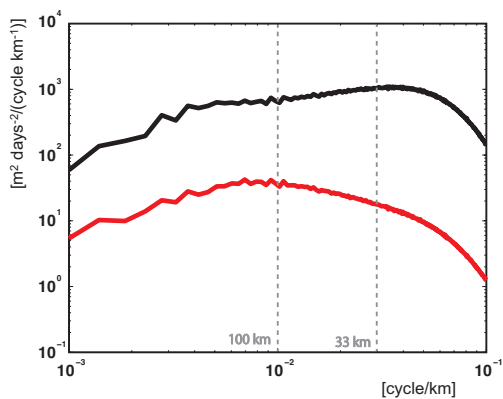
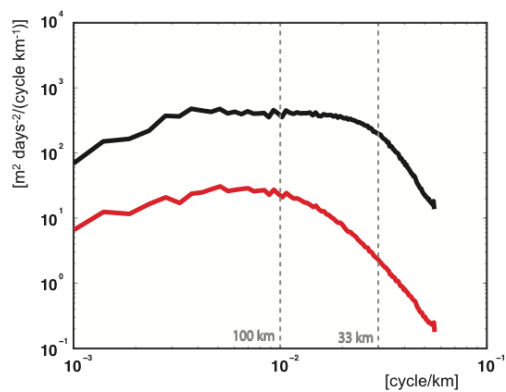


Figure 10

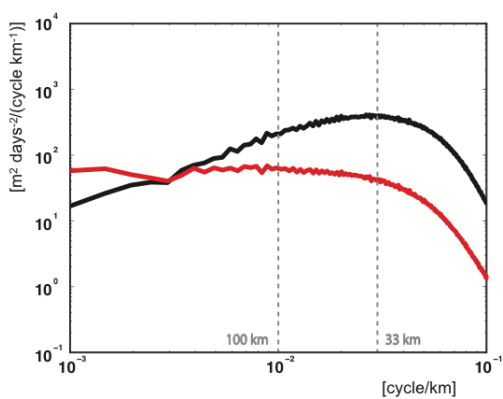
(a) KET, 1/30° simulation



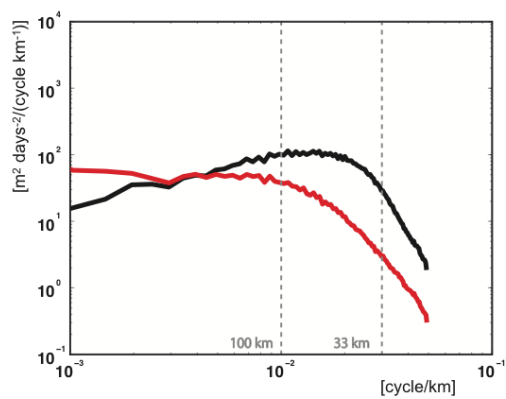
(b) KET, 1/10° simulation



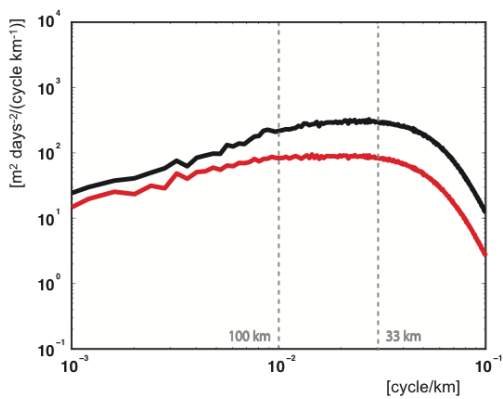
(c) STCC, 1/30° simulation



(d) STCC, 1/10° simulation



(e) STEP, 1/30° simulation



(f) STEP, 1/10° simulation

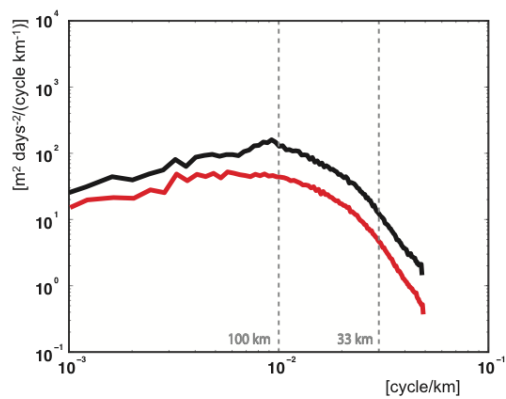
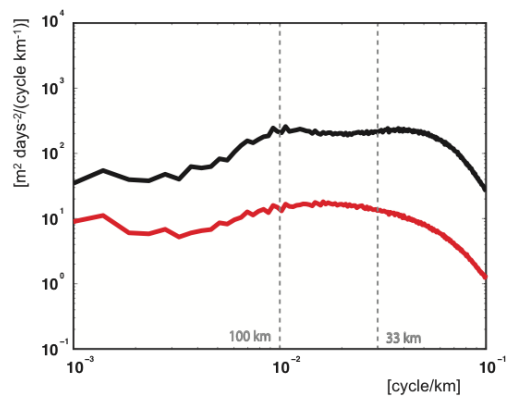
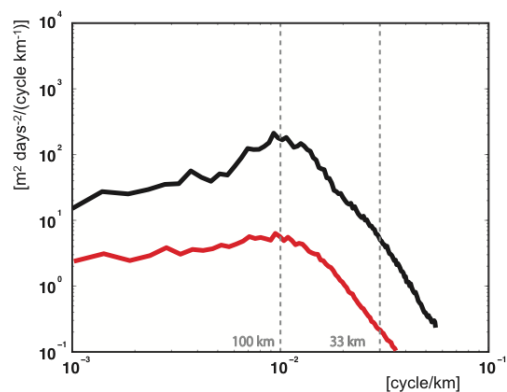


Figure 10

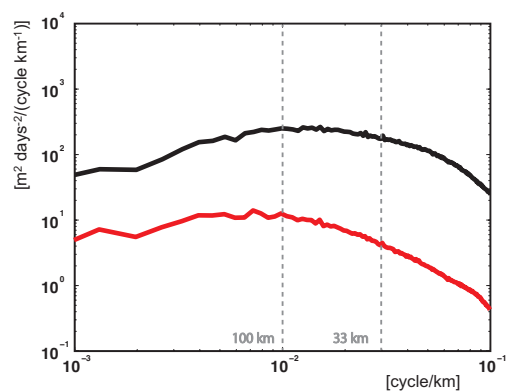
(g) MLEP, 1/30° simulation



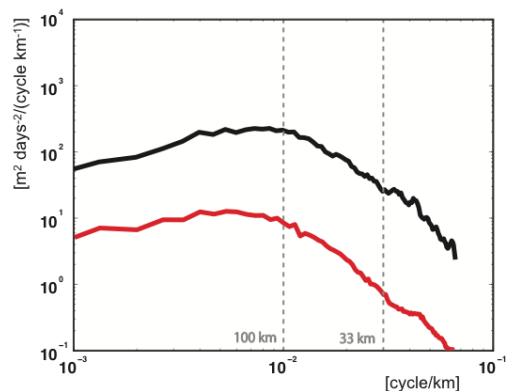
(h) MLEP, 1/10° simulation



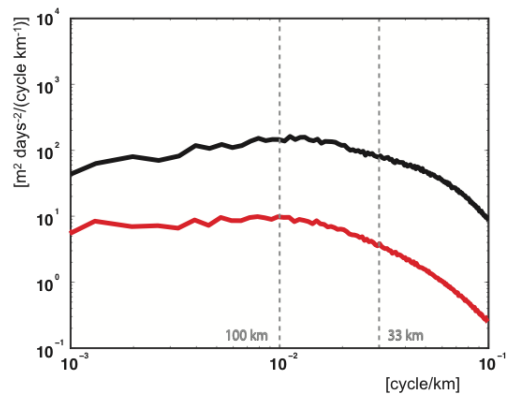
(i) SAWP, 1/30° simulation



(j) SAWP, 1/10° simulation



(k) SAEP, 1/30° simulation



(l) SAEP, 1/10° simulation

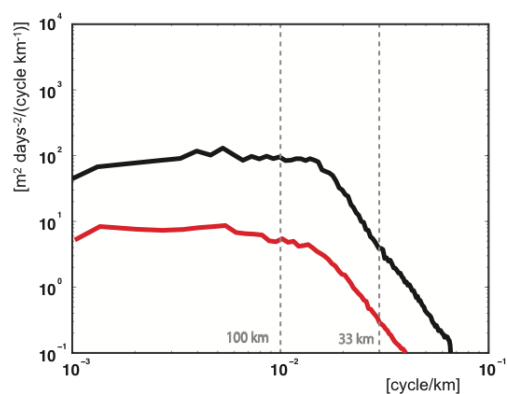
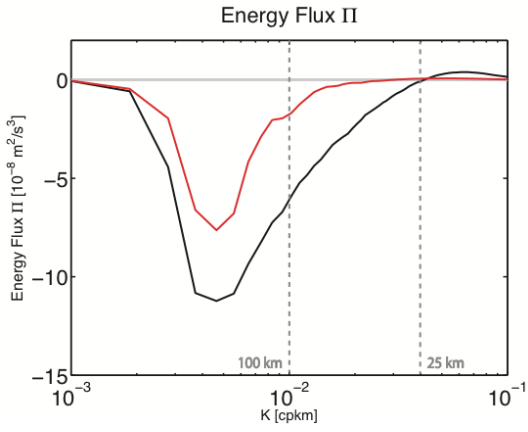
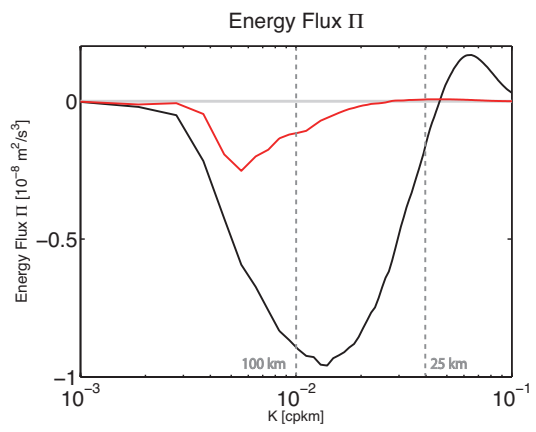


Figure 11

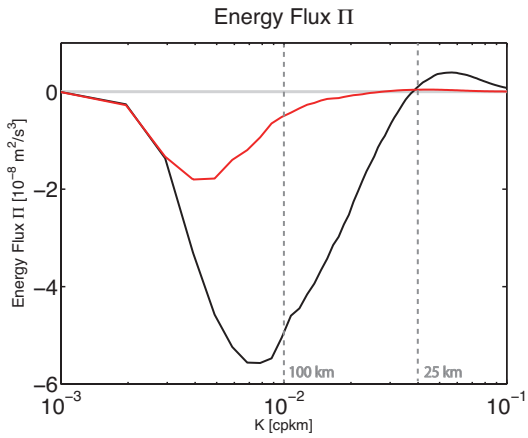
(a) KET



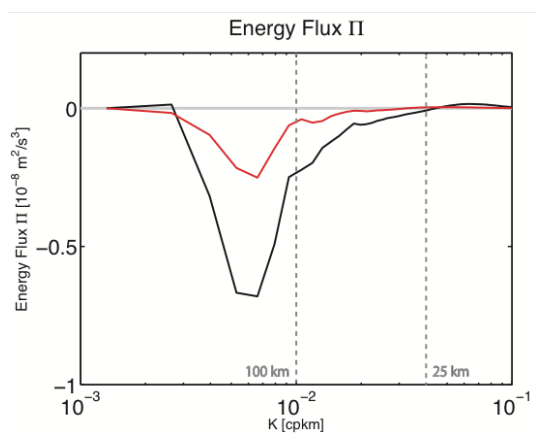
(d) MLEP



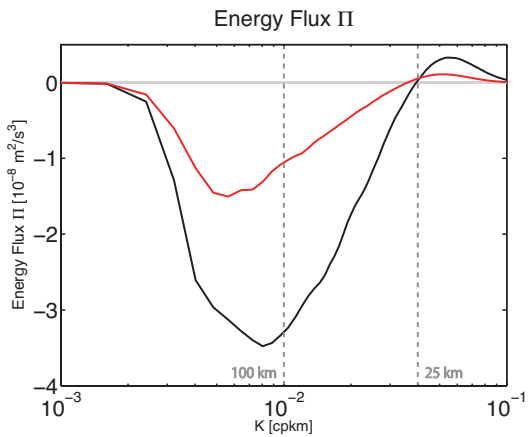
(b) STCC



(e) SAWP



(c) STEP



(f) SAEP

